Geophysical Journal International

Geophys. J. Int. (2013) **193,** 1166–1181
Advance Access publication 2013 April 04

doi: 10.1093/gji/ggt086

P-wave tomography for 3-D radial and azimuthal anisotropy of Tohoku and Kyushu subduction zones

Jian Wang[1,2] and Dapeng Zhao[2]

[1]*Key Laboratory of the Earth's Deep Interior, Institute of Geology and Geophysics, Chinese Academy of Sciences, Beijing* 100029, *China. E-mail: jianwang@mail.iggcas.ac.cn*
[2]*Department of Geophysics, Tohoku University, Sendai* 980–8578, *Japan. E-mail: zhao@aob.gp.tohoku.ac.jp*

Accepted 2013 March 4. Received 2013 February 24; in original form 2012 July 28

SUMMARY

We determined high-resolution *P*-wave tomography for 3-D radial and azimuthal anisotropy of the Tohoku and Kyushu subduction zones using a large number of high-quality arrival-time data of local earthquakes recorded by the dense seismic network on the Japan Islands. Trench-normal *P*-wave fast-velocity directions (FVDs) are revealed in the backarc mantle wedge in both Tohoku and Kyushu, which are consistent with the model of slab-driven corner flow. Trench-parallel FVDs with amplitude <4 per cent appear in the forearc mantle wedge under Tohoku and Kyushu, suggesting the existence of B-type olivine fabric there. Trench-parallel FVDs are also visible in the mantle wedge under the volcanic front in Tohoku but not in Kyushu, suggesting that 3-D flow may exist in the mantle wedge under Tohoku and the 3-D flow is affected by the subduction rate of the oceanic plate. Negative radial anisotropy (i.e. vertical velocity being faster than horizontal velocity) is revealed in the low-velocity zones in the mantle wedge under the arc volcanoes in Tohoku and Kyushu as well as in the low-velocity zones below the Philippine Sea slab under Kyushu, which may reflect hot upwelling flows and transitions of olivine fabrics with the presence of water in the upper mantle. Trench-parallel FVDs and positive radial anisotropy (i.e. horizontal velocity being faster than vertical velocity) are revealed in the subducting Pacific slab under Tohoku and the Philippine Sea slab under Kyushu, suggesting that the slabs keep their frozen-in anisotropy formed at the mid-ocean ridge or that the slab anisotropy is induced by the lattice-preferred orientation of the B-type olivine.

Key words: Seismic anisotropy; Seismic tomography; Subduction zone processes.

1 INTRODUCTION

Seismic anisotropy is induced mainly by the lattice-preferred orientation (LPO) of anisotropic minerals, especially olivine in the mantle (e.g. Hess 1964; Mainprice 2007). The olivine α-axis is generally assumed to be oriented nearly parallel to the flow direction, thus the observed fast shear-wave polarization direction is generally suggested to be parallel to the flow direction (e.g. Zhang & Karato 1995). However, many studies have suggested that the transitions of olivine fabric are induced by water content as well as temperature (e.g. Durham & Goetze 1977; Nicolas & Christensen 1987; Jung & Karato 2001; Katayama *et al.* 2004; Katayama & Karato 2006), pressure (e.g. Couvy *et al.* 2004; Mainprice *et al.* 2005; Raterron *et al.* 2007; Jung *et al.* 2009; Raterron *et al.* 2009; Ohuchi *et al.* 2011) and partial melting (e.g. Holtzman *et al.* 2003). In particular, fast shear-wave polarization direction is normal to the flow direction where the B-type olivine fabric is suggested to be dominant especially in the forcarc mantle wedge of subduction zones (Karato *et al.* 2008). B-type olivine fabric is also suggested to be formed in the high-stress, low-temperature slab-bending region near the trench, producing trench-parallel fast directions, with larger anisotropy formed in older slabs which require more extensive yielding to bend (Eberhart-Phillips & Reyners 2009). However, it is still in question for the conditions inducing the transition of olivine fabric from A-type to B-type (e.g. Couvy *et al.* 2004; Raterron *et al.* 2007; Karato *et al.* 2008; Jung *et al.* 2009).

Shear-wave splitting measurements frequently show trench-parallel fast polarization directions beneath many forearc areas (e.g. Smith *et al.* 2001; Nakajima & Hasegawa 2004; Pozgay *et al.* 2007; Huang *et al.* 2011a,b). The trench-parallel azimuthal anisotropy is possibly induced by the B-type olivine fabric dominating in the forearc mantle wedge of slab-driven corner flow (e.g. Katayama *et al.* 2004; Mizukami *et al.* 2004; Kneller *et al.* 2005), the extensively serpentinized mantle wedge rocks (e.g. Kern *et al.* 1997; Katayama *et al.* 2009; Boudier *et al.* 2010), or the 3-D flow in the mantle wedge (e.g. Behn *et al.* 2007;

Long & Silver 2008; Morishige & Honda 2011). However, Huang *et al.* (2011a) compared their shear-wave splitting measurements for local earthquakes in the subducting Pacific slab with those for the crustal earthquakes beneath the Tohoku forearc and suggested that the trench-parallel anisotropy exists mainly in the crust rather than in the mantle wedge, and so they pointed out that it is not necessary to attribute the trench-parallel shear-wave splitting to anisotropy in the forearc mantle wedge. Thus, it is hard to conclude that trench-parallel anisotropy does exist in the forearc mantle wedge with the shear-wave splitting measurements alone.

In Tohoku, the old Pacific Plate is subducting beneath the Okhotsk Plate from the Japan Trench at a rate of ∼9 cm yr^{-1} (Fig. 1b). In Kyushu, the relatively young Philippine Sea (PHS) Plate is subducting beneath the Eurasian Plate from the Nankai Trough at a rate of ∼5 cm yr^{-1} (Fig. 1d). Wang & Zhao (2008, 2012) investigated *P*-wave azimuthal anisotropy in Northeast Japan and Southwest Japan, respectively, but their models had a lower resolution, and so the *P*-wave anisotropy was not well resolved in the forearc mantle wedge under Tohoku and Kyushu. In this work, we developed a new tomographic method to determine the first 3-D *P*-wave radial anisotropy in both Tohoku and Kyushu subduction zones, as well as high-resolution *P*-wave tomography for 3-D azimuthal anisotropy in both regions. The high-resolution results of this work shed new light on the structure and dynamics of subduction zones.

2 METHOD AND DATA

The anisotropic media are common in the Earth's interior, which have been revealed by seismological observations and laboratory studies (e.g. Anderson & Dziewonski 1982; Crampin 1984; Thomsen 1986). However, a fully anisotropic medium with 21 independent elastic moduli is very difficult to deal with in both theory and practice. Fortunately, the anisotropy with hexagonal symmetry is a good approximation to the rocks in the Earth and reduces the number of free parameters (e.g. Christensen 1984; Park & Yu 1993; Maupin & Park 2007). For further simplification in geoscience, the hexagonal symmetry is generally assumed to be horizontal when the azimuthal anisotropy is concerned by the shear-wave splitting measurements (e.g. Savage 1999; Nakajima & Hasegawa 2004; Zhao & Xue 2010; Huang *et al.* 2011a,b) and *P*-wave velocity studies (e.g. Hess 1964; Backus 1965; Raitt *et al.* 1969; Hearn 1996; Eberhart-Phillips & Henderson 2004); whereas the hexagonal symmetry is generally assumed to be vertical when the radial anisotropy is concerned in the form of V_{sh}/V_{sv} variation (V_{sh} and V_{sv} are the velocities of horizontally and vertically polarized shear waves,

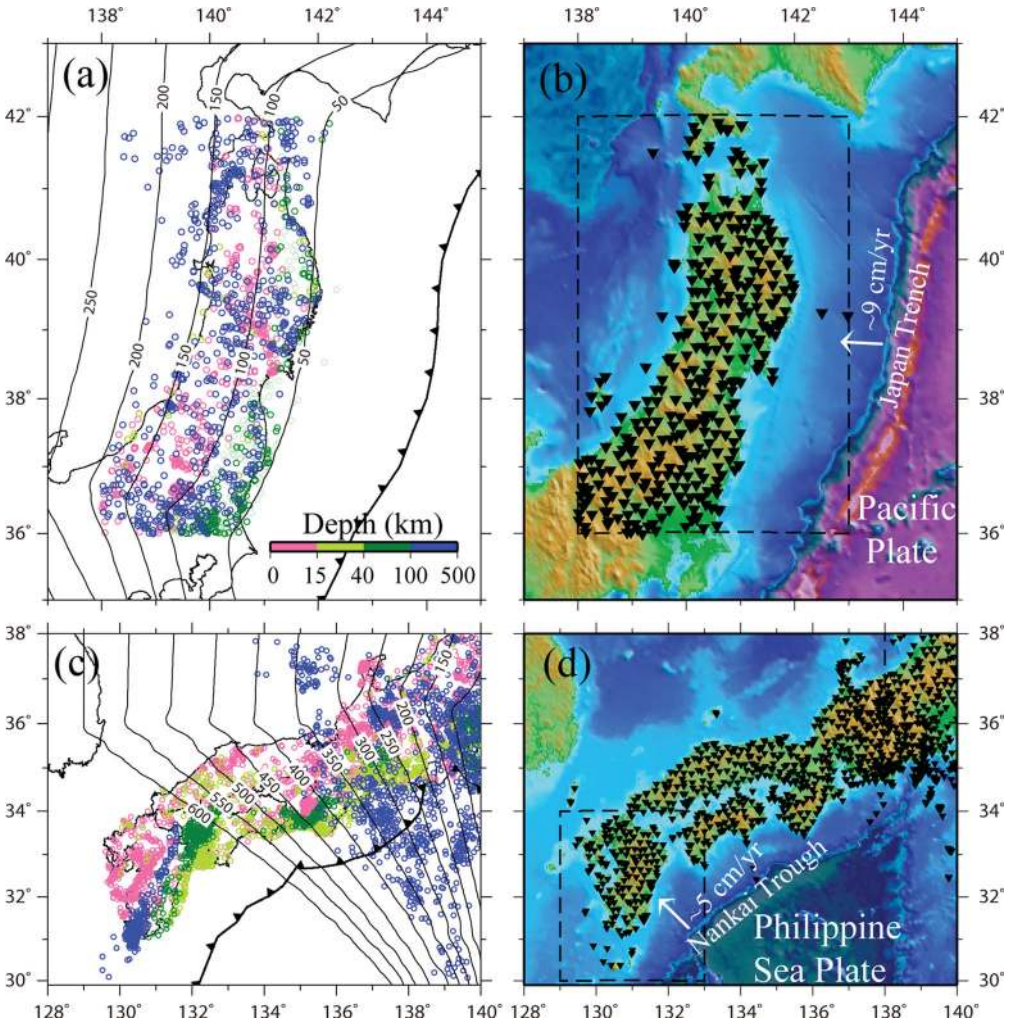

Figure 1. Distributions of the local earthquakes (a, c) and seismic stations (b, d) used in this study. The black boxes in (b) and (d) show the present study areas (Tohoku and Kyushu), plotted on a colour map of the topography (GTOPO30). The focal depths are shown in colour; its scale is shown in (a). The curved lines in (a, c) denote the depth contours of the upper boundary of the subducting Pacific slab.

respectively) in surface wave studies (e.g. Nettles & Dziewonski 2008; Fichtner *et al.* 2010; Yuan *et al.* 2011). In this work we have attempted to study 3-D *P*-wave radial and azimuthal anisotropy in the Japan subduction zone.

2.1 *P*-wave tomography for 3-D azimuthal anisotropy

To study the 3-D *P*-wave azimuthal anisotropy in Tohoku and Kyushu, we adopted the anisotropic tomography method of Wang & Zhao (2008, 2012) which was developed from the isotropic tomography method of Zhao *et al.* (1992), and the anisotropy method is similar to that of Eberhart-Phillips & Henderson (2004).

Following the formulation of Barclay *et al.* (1998) for hexagonal anisotropy based on θ, which is the angle between the propagation vector and the symmetry axis, the *P*-wave slowness can be expressed as

$$S = S_0 + M\cos(2\theta), \tag{1}$$

where S is the total slowness, S_0 is the average slowness (i.e. isotropic component), M is the parameter for anisotropy. For weak azimuthal anisotropy with a horizontal hexagonal symmetry axis (Fig. S1a), the *P*-wave slowness can be approximately expressed as (e.g. Backus 1965; Raitt *et al.* 1969; Hearn 1996; Eberhart-Phillips & Henderson 2004)

$$S(\phi) = S_0[1 + A_1\cos(2\phi) + B_1\sin(2\phi)], \tag{2}$$

where S is the total slowness, S_0 is the azimuthal average slowness, A_1 and B_1 are the azimuthal anisotropy parameters, ϕ is the ray path azimuth. The fast-velocity direction (FVD) ψ and the amplitude α of azimuthal anisotropy can be expressed as

$$\psi = \begin{cases} \frac{1}{2}\tan^{-1}\left(\frac{B_1}{A_1}\right) + \begin{cases} \frac{\pi}{2}, A_1 > 0 \\ 0, A_1 < 0, \end{cases} \\ -\frac{\pi}{4}, A_1 = 0, B_1 > 0, \\ \frac{\pi}{4}, A_1 = 0, B_1 < 0, \end{cases} \tag{3}$$

$$\alpha = \frac{V_f - V_s}{2V_0} = \frac{\sqrt{A_1^2 + B_1^2}}{1 - (A_1^2 + B_1^2)},$$

where V_0 denotes the average isotropic velocity, V_f and V_s denote the velocities in the fast and slow directions, respectively.

The relation between θ and the propagation vector could be defined as (Eberhart-Phillips & Henderson 2004)

$$\cos\theta = \sin i(\sin\phi\sin\psi + \cos\phi\cos\psi), \tag{4}$$

where i is the incident angle of ray path. Thus for local earthquakes within the modelling space, we have the following equation,

$$\begin{aligned} T_{mn}^{obs} - T_{mn}^{cal} = &\left(\frac{\partial T}{\partial\varphi}\right)_{mn}\Delta\varphi_n + \left(\frac{\partial T}{\partial\lambda}\right)_{mn}\Delta\lambda_n + \left(\frac{\partial T}{\partial h}\right)_{mn}\Delta h_n \\ &+ \Delta T_{0n} + \sum_p\left(\frac{\partial T}{\partial V_p}\Delta V_p\right) \\ &+ \sum_q\left(\frac{\partial T}{\partial A_{1q}}\Delta A_{1q} + \frac{\partial T}{\partial B_{1q}}\Delta B_{1q}\right) + E_{mn}, \end{aligned} \tag{5}$$

where T_{mn}^{obs} and T_{mn}^{cal} are the observed and calculated travel times from the nth event to the mth station, φ_n, λ_n, h_n and T_{0n} are the latitude, longitude, focal depth and origin time of the nth event, respectively, Δ denotes the perturbation of a parameter. Two 3-D grid nets are set up in the modelling space, one grid net is for expressing the 3-D isotropic velocity structure, whereas the other grid net is for expressing the 3-D anisotropy structure. In eq. (5), V_p is the isotropic velocity at the pth node of the first grid net, whereas A_{1q} and B_{1q} are the azimuthal anisotropy parameters at the qth node of the second grid net. E_{mn} represents higher-order terms of perturbations and errors in the data. The first four terms on the right side of eq. (5) are the contributions of the hypocentral parameters, which can be obtained using the method of Engdahl & Lee (1976). For details, see Eberhart-Phillips & Henderson (2004) and Wang & Zhao (2008).

2.2 *P*-wave tomography for 3-D radial anisotropy

We modified our tomography code for *P*-wave azimuthal anisotropy (Wang & Zhao 2008) to determine the 3-D *P*-wave radial anisotropy in Tohoku and Kyushu. If the hexagonal symmetry axis is vertical (Fig. S1b), eq. (1) could be rewritten as (Ishise *et al.* 2012)

$$\begin{aligned} S = S_0 + M\cos(2i) &= S_0\left[1 + \frac{M}{S_0}\cos(2i)\right] \\ &= S_0[1 + M_1\cos(2i)]. \end{aligned} \tag{6}$$

The amplitude β of radial anisotropy can be expressed as

$$\beta = \frac{V_{ph} - V_{pv}}{2V_0} = \frac{M_1}{1 - M_1^2}, \tag{7}$$

where V_{ph} and V_{pv} are the *P*-wave velocities in the horizontal and vertical directions, respectively. Thus, $\beta > 0$ represents that the horizontally propagating *P*-wave travels faster than the vertical one, that is, $V_{ph}/V_{pv} > 1$.

Using eq. (6), we can get traveltime T_k of the kth ray segment with length d as

$$\begin{aligned} &T_k = \mathrm{d}S = \mathrm{d}[1 + M_{1k}\cos(2i_k)]/V_k, \\ &T = \sum_k T_k, \end{aligned} \tag{8}$$

where T is the total traveltime of the ray, V_k is the isotropic velocity at the middle point of the kth ray segment, M_{1k} is the parameter for the radial anisotropy at the middle point of the kth ray segment, i_k is the incident angle of the kth ray segment. Thus, the partial derivatives to the velocity and radial anisotropy are expressed as

$$\begin{aligned} &\frac{\partial T}{\partial V_k} = -\mathrm{d}[1 + M_{1k}\cos(2i_k)]/V_k^2, \\ &\frac{\partial T}{\partial M_{1k}} = \frac{d}{V_k}\cos(2i_k). \end{aligned} \tag{9}$$

Similar to *P*-wave tomography for azimuthal anisotropy, V_k and M_{1k} at a point are calculated using linear interpolation of the parameters at the eight grid nodes surrounding that point. Then, the traveltime residual can be written as

$$\begin{aligned} T_{mn}^{obs} - T_{mn}^{cal} = &\left(\frac{\partial T}{\partial\varphi}\right)_{mn}\Delta\varphi_n + \left(\frac{\partial T}{\partial\lambda}\right)_{mn}\Delta\lambda_n + \left(\frac{\partial T}{\partial h}\right)_{mn}\Delta h_n \\ &+ \Delta T_{0n} + \sum_p\left(\frac{\partial T}{\partial V_p}\Delta V_p\right) \\ &+ \sum_q\left(\frac{\partial T}{\partial M_{1q}}\Delta M_{1q}\right) + E_{mn}. \end{aligned} \tag{10}$$

Eqs (5) and (10) are solved using the LSQR algorithm (Paige & Saunders 1982).

2.3 Data and model setup

We used ∼150 000 high-quality *P*-wave arrival times from 1858 local shallow and intermediate-depth earthquakes (Fig. 1a) recorded by 381 seismic stations (Fig. 1b) in Tohoku. For studying *P*-wave anisotropic structure in and around the PHS slab, we used ∼560 000 *P*-wave arrival times from 5249 local earthquakes (Fig. 1c) recorded by 1088 seismic stations (Fig. 1d) in Southwest Japan. These local events occurred during 2003 January to 2007 June and the first *P*-wave arrival-time data were collected from original seismograms with accuracy of 0.05–0.1 s by the staffs of Research Center for Prediction of Earthquakes and Volcanic Eruptions, Tohoku University.

Following the previous studies of the Japan subduction zone (e.g. Zhao *et al.* 1992, 2012; Wang & Zhao 2008, 2012), a slightly modified J-B velocity model (Jeffreys & Bullen 1940) was adopted as the starting velocity model, and the depth variations of the Conrad and Moho discontinuities and the upper boundary of the subducting Pacific slab were taken into account. The Pacific slab was assumed to be 85 km thick and with 4 per cent faster *P*-wave velocity than that of the surrounding mantle in the starting velocity model. A 3-D net of grid nodes with a horizontal interval of 0.25° and at depths of 0, 10, 25, 40, 60, 80, 100, 120, 150, 180, 210, 240, 270 and 300 km was set for both isotropic velocity variation and anisotropy.

3 RESOLUTION ANALYSIS

We conducted the checkerboard resolution tests (CRTs; Zhao *et al.* 1992) to confirm the main features of the obtained *P*-wave anisotropic tomography. In the input model of CRTs for azimuthal anisotropy tomography, isotropic velocity anomalies of ±4 per cent are alternatively assigned to the grid nodes, the FVDs at two adjacent grid nodes are perpendicular to each other (22.5° and 112.5°) with anisotropy amplitude of 2.8 per cent. Random errors in a normal distribution with a standard deviation of 0.1 s were added to the theoretical arrival times calculated for the CRT input model. Figs 2 and 3 show the recovered images beneath the Tohoku and Kyushu districts, respectively. The results of the CRTs show that the resolution is generally good at depths <100 km, where trench-parallel

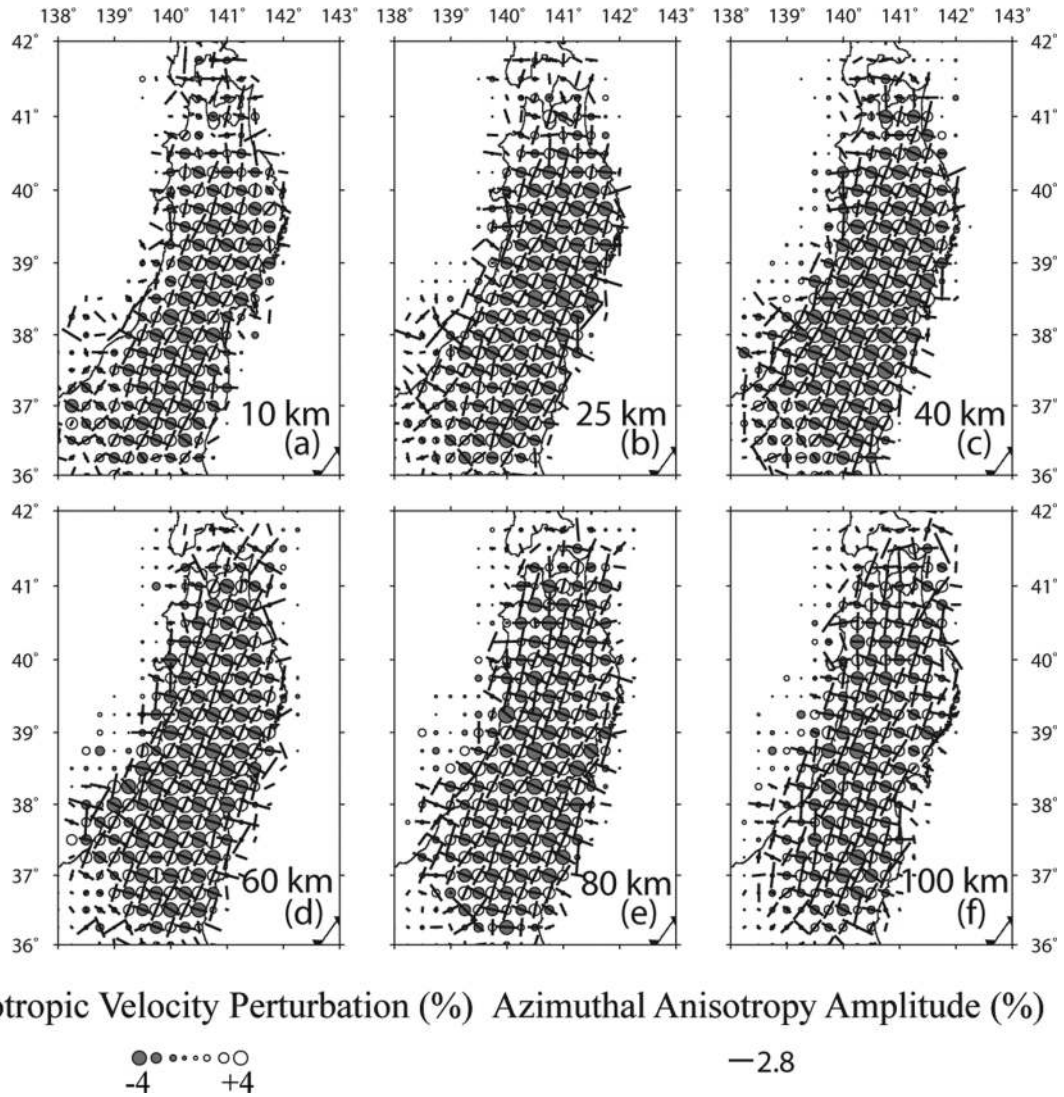

Figure 2. Results of a checkerboard resolution test for *P*-wave azimuthal anisotropy in Tohoku. In the input model, isotropic velocity anomalies of ±4 per cent are assigned alternatively to the grid nodes, and the fast-velocity directions (FVDs) at two adjacent grid nodes are perpendicular to each other (22.5° and 112.5°) with anisotropic amplitude of 2.8 per cent. Black and white circles denote low and high velocity perturbations, respectively. The azimuth and length of bars represent the FVD and azimuthal anisotropy amplitude, respectively. The scales are shown at the bottom.

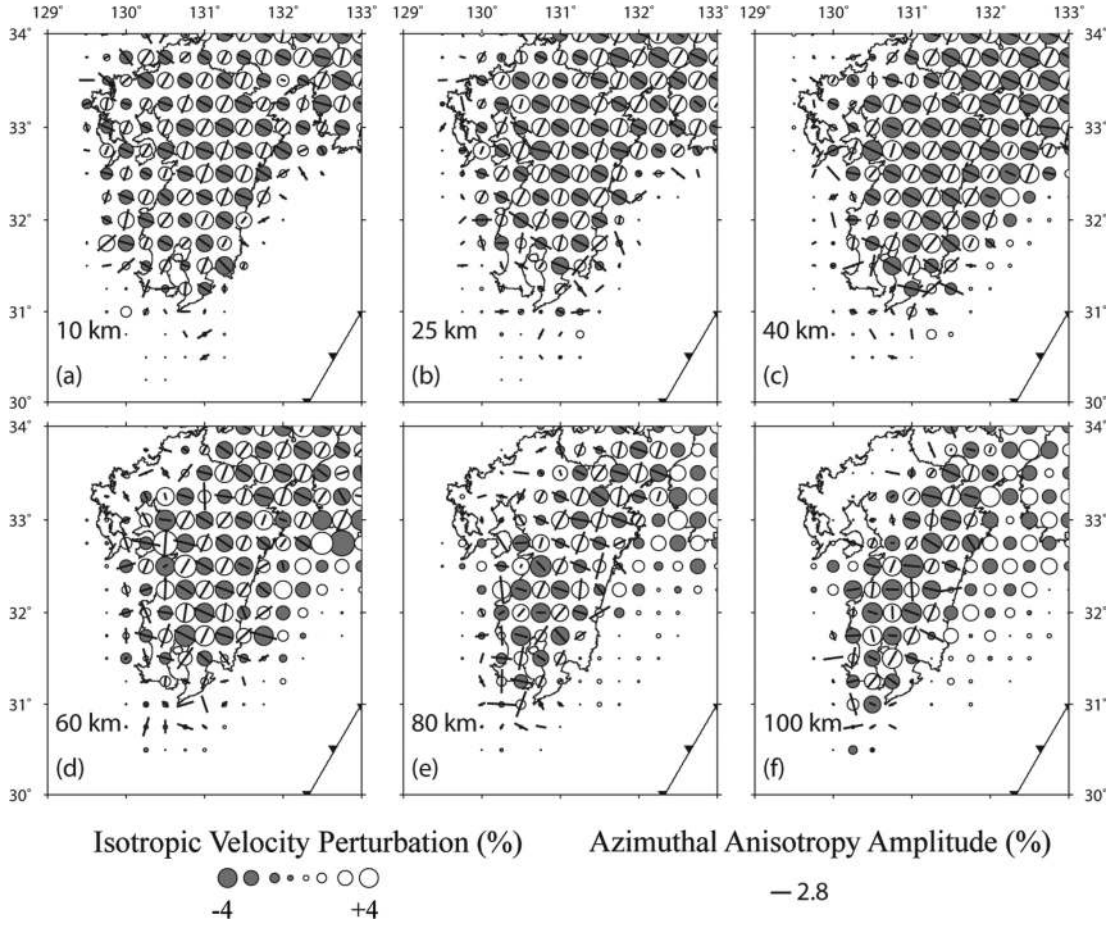

Figure 3. The same as Fig. 2 but for the results of a checkerboard resolution test in Kyushu.

anisotropy was assumed to exist in the forearc mantle wedge (e.g. Nakajima & Hasegawa 2004; Jung *et al.* 2006; Karato *et al.* 2008). The recovered amplitude of the azimuthal anisotropy is nearly equal to the input one (2.8 per cent). The anisotropic amplitude is affected by the chosen damping parameter (Wang & Zhao 2008). The inversion results were obtained after four iterations, and the damping parameters for the anisotropic parameter were chosen to be 4.0, 8.0, 12.0 and 16.0 in the four iterations to avoid the underdamped inversion. Fig. S2 shows the CRT result in Kyushu with a damping parameter 2.0 in the four iterations, and the anisotropic amplitude becomes very large at some grid nodes, suggesting that the anisotropic amplitude is affected significantly by the chosen damping parameter. Hence we have made great efforts to conduct many inversions so as to find the optimal value of the damping parameter.

We also conducted similar CRTs for the radial anisotropy tomography. In the input model of the CRT, isotropic velocity anomalies of ± 4 per cent and radial anisotropy amplitude of ± 3 per cent were alternatively assigned to the grid nodes in the input model for the radial anisotropy tomography. Random errors in a normal distribution with a standard deviation of 0.1 s were also added to the theoretical arrival times. Figs 4 and 5 show the recovered images of the checkerboard model in Tohoku and Kyushu, which indicate that the resolution is very good at depths <100 km.

Although it is concerned that the inverted seismic anisotropy could be induced by the unresolved structural heterogeneity (e.g. Capdeville *et al.* 2010; Fichtner *et al.* 2010), the synthetic tests of our previous studies (Wang & Zhao 2012, 2013) as well as the presents ones show that the *P*-wave anisotropy can certainly be distinguished from the velocity heterogeneity by our inversion algorithm when a great amount of high-quality arrival-time data recorded by a dense seismic network are used, such as the superb data set used in this study.

4 RESULTS

4.1 Tohoku subduction zone

Fig. 6 shows map views of the obtained *P*-wave azimuthal anisotropy tomography under Tohoku. The anisotropic pattern in the upper mantle is generally consistent with that of the previous studies, that is, trench-parallel FVDs appear in the forearc mantle wedge and the subducting Pacific slab, while trench-normal FVDs exist in the backarc mantle wedge (Wang & Zhao 2008, 2010; Cheng *et al.* 2011; Huang *et al.* 2011c).

Fig. 7 shows a comparisons of the *P*-wave FVDs at 10 km depth (red bars) with the *S*-wave polarizations (blue bars) of the crustal events (Huang *et al.* 2011a) in Tohoku. Under the forearc area, both the *P*-wave FVDs and the *S*-wave polarizations are primarily trench-parallel (nearly N–S direction), which are consistent with the N–S strikes of the active reverse faults in Tohoku (for information on the active faults, see the website http://riodb02.ibase.aist.go.jp/activefault/cgi-bin/search.cgi?%20search). The main difference is that *S*-wave polarizations exhibit NWW-SEE FVDs in the volcanic area, which are suggested to be parallel to the tectonic stress by Huang *et al.* (2011a). However, our

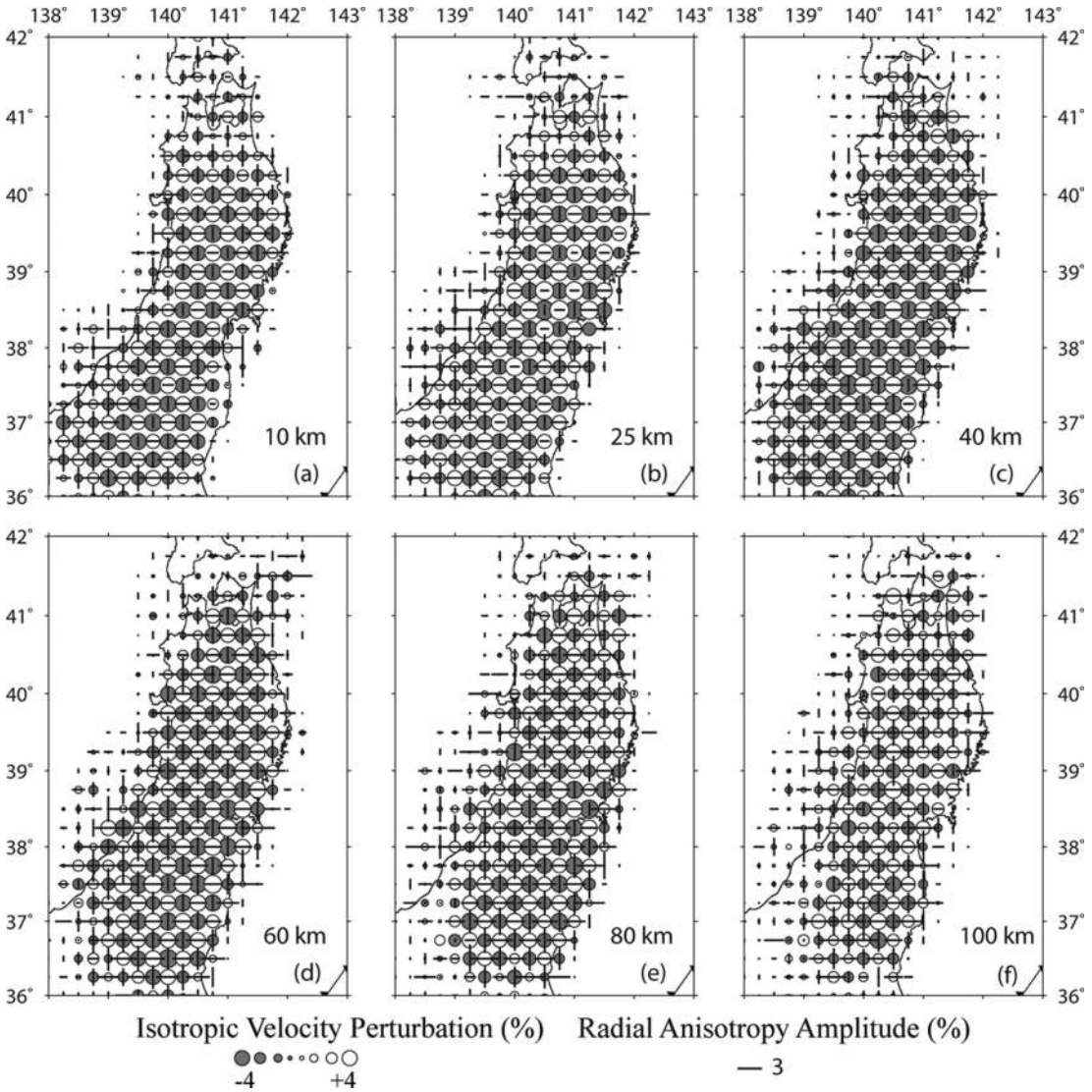

Figure 4. Results of a checkerboard resolution test for *P*-wave radial anisotropy in Tohoku. Isotropic velocity anomalies of ±4 per cent and radial anisotropy amplitude of ±3 per cent are assigned alternatively to the grid nodes in the input model. Black and white circles denote low and high velocity perturbations, respectively. The horizontal bars denote that the horizontal velocity is greater than the vertical velocity at each grid node, whereas the vertical bars denote that the vertical velocity is greater than the horizontal velocity at each grid node. The length of bars denotes the radial anisotropy amplitude. The scales are shown at the bottom.

previous results (Wang & Zhao 2008, 2010) showed complex and nearly random *P*-wave FVDs in the upper crust. The comparison suggests that the *P*-wave anisotropic tomography needs a very high resolution to image the small-scale anisotropy induced mainly by microcracks and cracks in the upper crust.

Fig. 8 shows comparisons of the obtained *P*-wave FVDs (red bars) at six depths under Tohoku with the *S*-wave polarizations (blue bars) of local intermediate-depth earthquakes in the Pacific slab measured by Huang *et al.* (2011a; Figs 8a–f) and by Nakajima & Hasegawa (2004) and Nakajima *et al.* (2006; Figs 8g–l). Our present *P*-wave azimuthal anisotropy shows some new features. In the lower crust (25 km depth), the *P*-wave FVDs are complex but become trench-parallel near the Pacific coast. In the upper mantle, the *P*-wave FVDs are generally trench-normal under the backarc area, whereas they become nearly trench-parallel in the Pacific slab, in the forearc mantle wedge at 40 km depth and beneath the volcanic front area at depths of 60–100 km (Figs 6 and 8). The trench-parallel *P*-wave FVDs in the forearc mantle wedge are imaged clearly at 40 km depth with anisotropic amplitude of 2–3 per cent. In addition, the trench-parallel FVDs appear in the Pacific slab and the mantle wedge at 80 and 100 km depths with anisotropic amplitude of 2–4 per cent. However, trench-normal *P*-wave FVDs become dominant in the forearc mantle wedge at 60 km depth. Our present results show that the trench-parallel anisotropy in the forearc mantle wedge is weak beneath Tohoku, which is consistent with the conclusion of Huang *et al.* (2011a) that the *S*-wave splitting delay times of crustal earthquakes make up ∼80 per cent of the total delay times of the slab earthquakes under Tohoku.

Beneath the volcanic area in Tohoku, the *P*-wave FVDs are generally trench-normal with anisotropic amplitude of ∼2 per cent at 40 km depth, whereas they become nearly trench-parallel with anisotropic amplitudes of ∼1 per cent at 60 km depth, very weak at 80 km depth, and increasing to ∼2 per cent close to the Pacific slab at 100 km depth. However, these anisotropic features are not visible in the shear-wave splitting measurements (Fig. 8) because they have poor depth resolution.

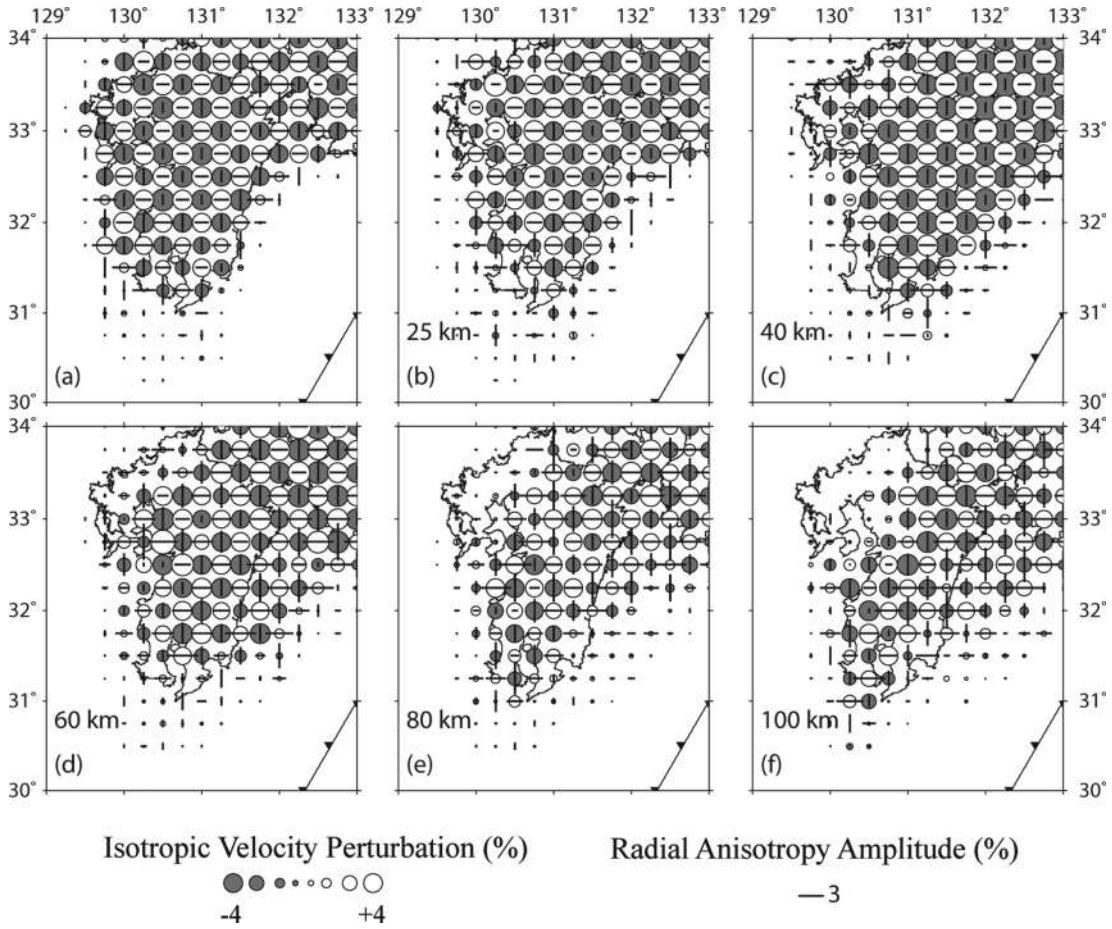

Figure 5. The same as Fig. 4 but for the results of a checkerboard resolution test in Kyushu.

Fig. 9 shows six east–west vertical cross-sections of *P*-wave radial anisotropy tomography under Tohoku. We can see that negative radial anisotropy ($\beta < 0$, i.e. vertical velocity > horizontal velocity, as shown in vertical bars) generally appears in the low-velocity (low-V) zones in the mantle wedge under the volcanic front and the backarc region. In contrast, positive radial anisotropy ($\beta > 0$, i.e. horizontal velocity > vertical velocity, as shown in horizontal bars) generally appears in the subducting Pacific slab and high-velocity (high-V) zones in the mantle wedge. However, the positive radial anisotropy ($\beta > 0$) is also visible in some low-V zones in the forearc mantle wedge as well as in a few low-V zones in the deeper portion of the mantle wedge directly above the Pacific slab. As a whole, the amplitude of the *P*-wave radial anisotropy is smaller than 5 per cent in the upper mantle.

4.2 Kyushu subduction zone

Fig. 10 shows map views of the obtained *P*-wave azimuthal anisotropy tomography under Kyushu. The *P*-wave FVDs are very complex in the crust, while they are trench-normal in the backarc mantle wedge and trench-parallel in the subducting PHS slab which is clearly visible as a high-V zone. This pattern is similar to that of a previous study of Southwest Japan (Wang & Zhao 2012). The *P*-wave FVDs are generally trench-parallel with anisotropy amplitude of 1–3 per cent in the forearc mantle wedge at depths of 40–80 km, which was not revealed by Wang & Zhao (2012) because of the lower resolution of their model. The trench-parallel *P*-wave FVD with anisotropy amplitude of ∼4 per cent is imaged in the subducting PHS slab south of ∼32.7°N, where the slab is older than 50 Ma.

Shear-wave splitting measurements of the intermediate-depth earthquakes in the PHS slab revealed dominant E–W (trench-normal) FVDs with delay times of ∼0.5 s in both the forearc and backarc areas beneath middle-south Kyushu (Salah *et al.* 2009). However, trench-parallel *S*-wave polarization with delay time of ∼1 s was revealed in the forearc beneath Kyushu using teleseismic shear waves (S, SKS and SKKS) recorded by the F-net broadband array (Long & van der Hilst 2005). Our present results show that the trench-parallel anisotropy does exist in the forearc mantle wedge and the subducting PHS slab beneath Kyushu.

Fig. 11 shows five vertical cross-sections of *P*-wave radial anisotropy tomography beneath Kyushu. The images under Kyushu are very similar to those under Tohoku (Fig. 9) that negative radial anisotropy ($\beta < 0$, as shown in vertical bars) generally exists in the low-V zones, whereas positive radial anisotropy ($\beta > 0$, as shown in horizontal bars) is prominent in the subducting PHS slab (the high-V zones).

4.3 Synthetic tests

To further examine the reliability of our *P*-wave anisotropy tomography, we conducted two synthetic tests to investigate the possible trade-off between heterogeneity and anisotropy in our tomographic inversions. In the first test, similar to the CRT as mentioned above, isotropic velocity perturbations of ±4 per cent were alternatively assigned to the grid nodes but neither azimuthal nor

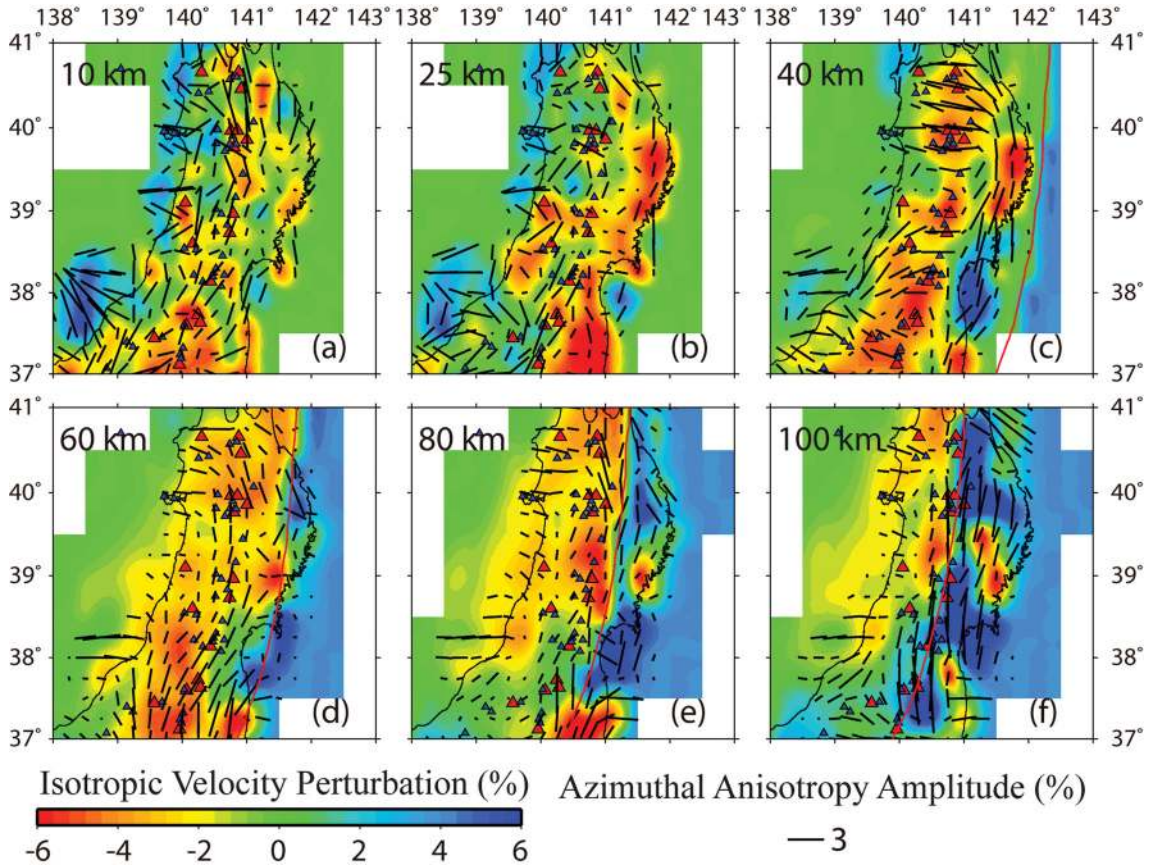

Figure 6. Map views of *P*-wave azimuthal anisotropy tomography at six depths under Tohoku. Red and blue colors denote low and high isotropic-velocity anomalies, respectively. The azimuth and length of each bar represent the *P*-wave fast-velocity direction and the anisotropy amplitude, respectively. Red curved lines show the upper boundary of the subducting Pacific slab at each depth. Red and blue triangles denote the active and quaternary volcanoes, respectively. The scales are shown at the bottom.

radial anisotropy were considered in the input model. The inverted images are shown in Figs S3–S6. In the second test, the input model contains 2.8 per cent azimuthal anisotropy or 3 per cent radial anisotropy without the isotropic velocity anomaly, and the inverted results are shown in Figs S7–S10. Although no anisotropy or isotropic velocity anomaly was included in the input model, ghost anisotropy or isotropic velocity anomalies do appear in the inversion results because of the trade-off between anisotropy and heterogeneity. However, the ghost anisotropy or isotropic velocity anomalies appearing in the inversion results are very weak and generally have amplitudes of <1.0 per cent, indicating that the influence of the trade-off is very small in our results, thanks to the excellent data set used in this study.

To confirm the main features of the inverted results, we made two more synthetic tests. In the first test, the input model was constructed from the obtained inversion result. Random errors in a normal distribution with a standard deviation of 0.15 s were added to the theoretical arrival times calculated for the synthetic input model. The inversion results of the synthetic test (Figs S11–S14) show that the main anisotropic features in Tohoku and Kyushu are well reconstructed, for example, trench-normal FVDs in the backarc, trench-parallel FVDs in the forearc and the subducting slabs, negative radial anisotropy dominant in the low-V zones, and positive radial anisotropy dominant in the high-V zones. The second test was made to judge whether there is a tendency that the negative radial anisotropy is coupled with the low-V anomaly, and the positive radial anisotropy is coupled with the high-V anomaly. The input model contained the same isotropic velocity anomalies of the real inversion result but the radial anisotropy opposite to the real results. That is, positive radial anisotropy was imposed in the low-V zones, while negative radial anisotropy was assigned in the high-V zones (Figs S15 and S16). The radial anisotropy amplitude is ± 3 per cent in the input model. The inversion results of the synthetic test (Figs S17 and S18) show that the pattern of radial anisotropy in the input model is well recovered.

The results of these synthetic tests indicate that the main features of the *P*-wave azimuthal and radial anisotropy (Figs 6 and 9–11) are well resolved and so they are reliable features, thanks to the great number of high-quality data and the excellent crisscrossing of rays which were recorded by the dense seismic network on the Japan Islands.

5 DISCUSSION

5.1 Azimuthal anisotropy in the mantle wedge

Trench-normal *P*-wave FVDs, observed in the backarc mantle wedge beneath both Tohoku and Kyushu, are consistent with the model in which the olivine α-axis aligns with the slab-driven corner flow, which is similar to the previous studies (e.g. Wang & Zhao 2008, 2012; Eberhart-Phillips & Reyners 2009; Huang *et al.* 2011c).

We think that trench-parallel *P*-wave FVDs do exist in the forearc mantle wedge in both Tohoku and Kyushu due to the following considerations. (1) Our azimuthal anisotropy result accords with

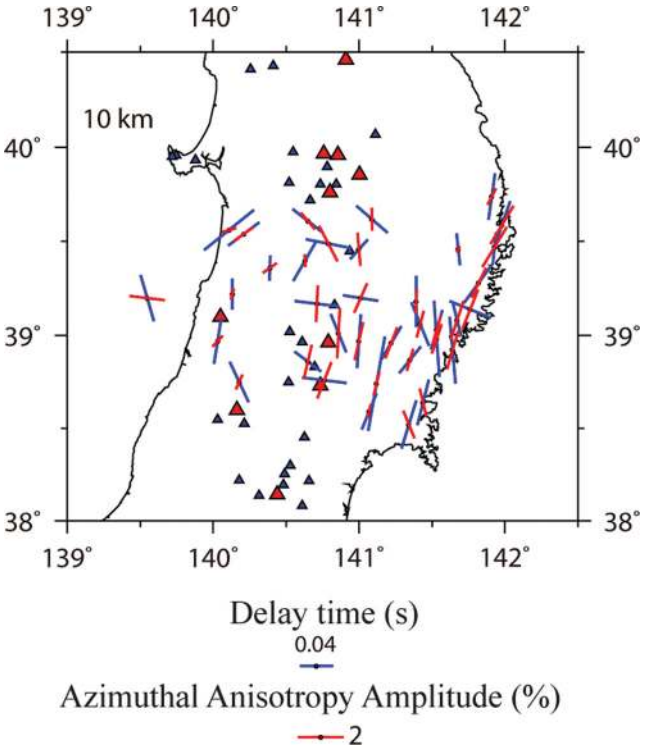

Figure 7. Distributions of the *P*-wave fast-velocity directions (FVDs) in the crust determined by this study (red bars) and the shear-wave splitting measurements of local crustal earthquakes by Huang *et al.* (2011a) (blue bars). Red and blue triangles denote the active and quaternary volcanoes, respectively. The azimuth of each bar represents the FVD, whereas the bar length denotes the *S*-wave delay time at each station or the *P*-wave anisotropy amplitude; their scales are shown at the bottom.

the model in which the olivine α-axis aligns with the trench-parallel flow above the subducting slab. Some studies (e.g. Russo & Silver 1994; Smith *et al.* 2001; Long & Silver 2008) suggested trench migration as the cause of the trench-parallel flow near the trench. However, Karato *et al.* (2008) pointed out that it is difficult to produce trench-parallel flow there because the velocity of trench migration is much smaller than that of slab subduction in most cases. (2) The trench-parallel azimuthal anisotropy supports the hypothesis of B-type olivine fabric dominant there with high water content in the olivine and at low temperature (e.g. Katayama *et al.* 2004; Kneller *et al.* 2005; Jung *et al.* 2006; Karato *et al.* 2008). (3) The trench-parallel azimuthal anisotropy may be induced by the LPO of serpentine in the forearc mantle wedge. The serpentinization could occur in the forearc mantle wedge because of large volumes of water releasing upwards into the mantle wedge from dehydration of the subducting oceanic crust and sediments at ~50 km depth (e.g. Bostock *et al.* 2002; Carlson & Miller 2003; Hyndman & Peacock 2003; Xia *et al.* 2008; Tong *et al.* 2011, 2012; Liu *et al.* 2013). However, the anisotropic amplitude of serpentine (~32 per cent) is much larger than that of olivine (3–5 per cent; e.g. Christensen 2004; Watanabe *et al.* 2007; Katayama *et al.* 2009). Our present results show that the azimuthal anisotropic amplitude is not larger than 5 per cent in the mantle. Thus, we consider that the content of serpentine should be small and the main contribution to anisotropy should come from olivine in the mantle wedge. Although solubility studies (e.g. Keppler & Bolfan-Casanova 2006; Grant *et al.* 2007) suggested that only small amounts of water may be incorporated in olivine at low pressure, the trench-parallel anisotropy in the forearc mantle wedge above the subducting slabs is more likely caused by the LPO of B-type olivine due to the presence of water.

However, the trench-parallel *P*-wave FVDs in the forearc mantle wedge exist at the shallow part (40 km depth) under Tohoku (Fig. 6), while they appear continuously at depths of 40–80 km under Kyushu (Fig. 10). In addition, our results show that the trench-parallel *P*-wave FVDs exist beneath the volcanic front area in Tohoku but not in Kyushu. The discontinuity of the trench-parallel anisotropy beneath the volcanic front area and in the forearc mantle wedge at 60 km depth (Figs 6d, 7d and j) suggests that the B-type olivine fabric could not explain the trench-parallel anisotropy beneath the volcanic front area in Tohoku. A plausible explanation for the trench-parallel anisotropy beneath the volcanic front is that the anisotropy reflects 3-D flow in the mantle wedge (e.g. Honda & Yoshida 2005; Behn *et al.* 2007; Morishige & Honda 2011). The 3-D flow in the mantle wedge, if any, may be caused by oblique convergence (Hall *et al.* 2000), slab rollback (Kincaid & Griffiths 2003), low viscosity wedge (Honda & Yoshida 2005), or foundering of arc lower crust (Kay & Kay 1991; Behn *et al.* 2007). Although the factors causing 3-D flow in the mantle wedge are still in question, foundering of the arc lower crust seems consistent with our present anisotropic results. Many studies (e.g. Kay & Kay 1991; Jull & Kelemen 2001) have suggested that the crustal assemblages would be denser than the underlying mantle at conditions suitable for the arc lower crust (800°–1000° and 1 GPa; Kelemen *et al.* 2003). The denser lower crust would become gravitationally unstable and sink into the mantle (Jull & Kelemen 2001; Behn *et al.* 2007). We think that the great compression by the Pacific Plate subduction at a rate of ~9 cm yr^{-1} would result in a denser lower crust and cause 3-D flow in the mantle wedge under the volcanic front in Tohoku, and as a result, the 3-D flow would produce relatively weak (~1 per cent at 60 km depth and <1 per cent at 80 km depth) trench-parallel azimuthal anisotropy there. Our present results suggest that a denser lower crust may not be formed by the PHS Plate subduction at a smaller rate of ~5 cm yr^{-1} in Kyushu.

5.2 Azimuthal anisotropy in the subducting slabs

Trench-parallel azimuthal anisotropy exists in the subdcting Pacific slab under Tohoku and in the PHS slab under Kyushu, which is consistent with the previous studies (e.g. Ishise & Oda 2005; Wang & Zhao 2008, 2010, 2012; Eberhart-Phillips & Reyners 2009; Huang *et al.* 2011c). Recently, Tian & Zhao (2012) determined *P*-wave anisotropic tomography of the Alaska subduction zone and found that trench-normal anisotropy exists within the subducting Pacific slab which is relatively young.

There are several possibilities for the generation of trench-parallel anisotropy in the slab: (1) a thick serpentinized shear zone atop the subducting slabs (Katayama *et al.* 2009) or serpentine-filled fractures in subducting slabs (Faccenda *et al.* 2008); (2) trench-parallel normal faults and cracks developed in the upper part of the subducting slab (Faccenda *et al.* 2008; Huang *et al.* 2011c); (3) frozen-in anisotropy when the oceanic plate was formed (Ishise & Oda 2005; Wang & Zhao 2008, 2012; Tian & Zhao 2012) and (4) B-type olivine fabric formed in the slab through high-stress slab bending in the trench region (Eberhart-Phillips & Reyners 2009).

For the first possibility, the contribution to anisotropy from serpentine should be small in Tohoku and Kyushu, as mentioned above. The second possibility may apply to the trench-parallel anisotropy in the uppermost part of the subducting slabs but not to the entire slabs under Tohoku and Kyushu. The third possibility seems to be suitable for the trench-parallel anisotropy within the Pacific slab

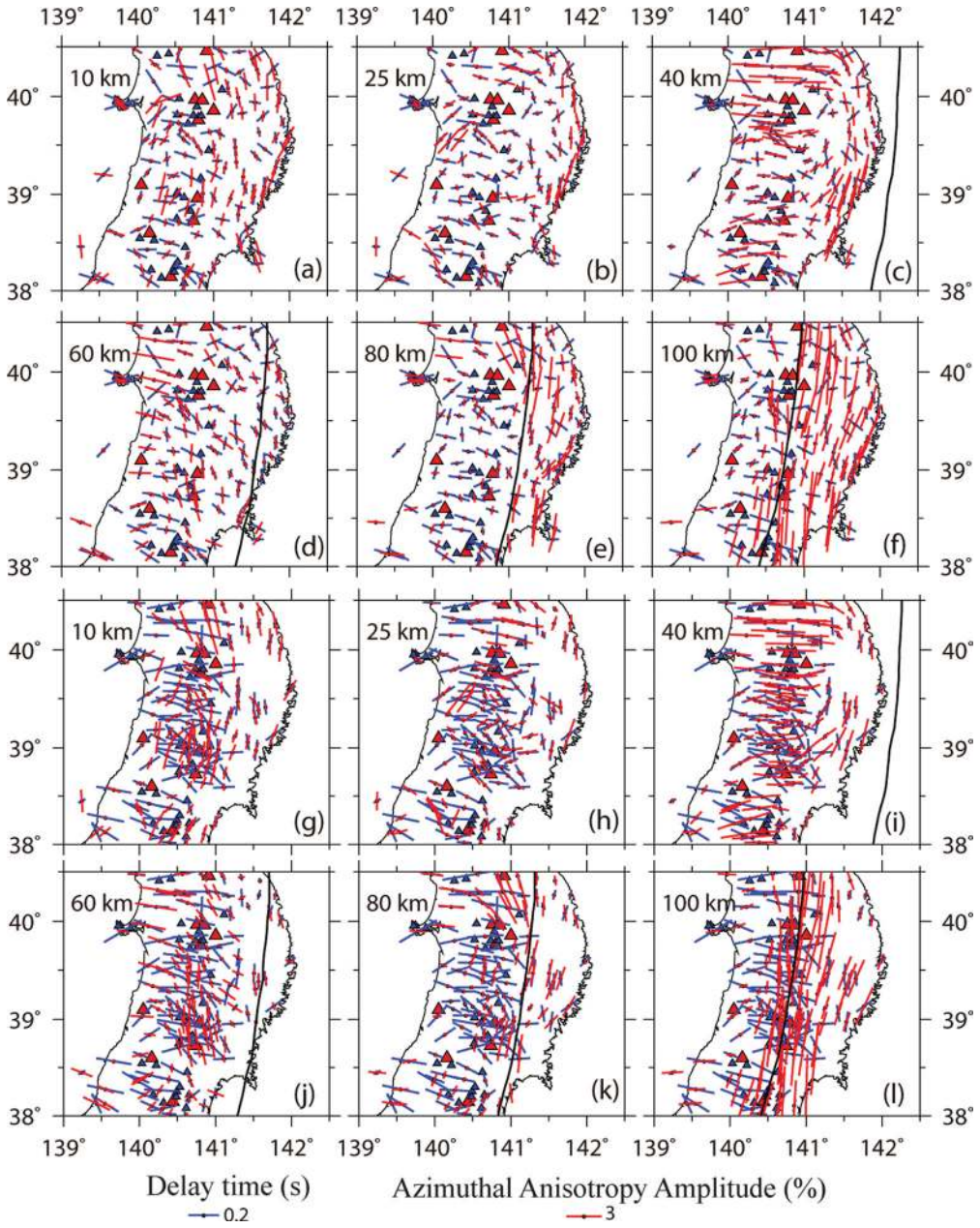

Figure 8. Distribution of the *P*-wave fast-velocity directions (FVDs) at each depth determined by this study (red bars). The blue bars denote the shear-wave splitting measurements of local intermediate-depth earthquakes in the subducting Pacific slab by Huang *et al.* (2011a) in (a–f) and by Nakajima & Hasegawa (2004) and Nakajima *et al.* (2006) in (g–l). Red and blue triangles denote the active and quaternary volcanoes, respectively. The azimuth of each bar represents the FVD, whereas the bar length denotes the *S*-wave delay time at each station or the *P*-wave anisotropy amplitude; their scales are shown at the bottom. The black curved lines denote the upper boundary of the subducting Pacific slab at each depth.

under Tohoku and the PHS slab under Kyushu, as well as for the trench-normal anisotropy within the Pacific slab in Alaska (Tian & Zhao 2012). These FVDs are nearly normal to the magnetic lineations in ocean floors close to the trenches (Hess 1964; Weissel *et al.* 1981). However, the magnetic lineations are NEE-SWW in the Pacific Ocean floor east of the Japan Trench, which are roughly perpendicular to the inverted N–S (trench-parallel) FVDs in the subducting Pacific slab beneath Tohoku. Although NW–SE shear-wave splittings were suggested to exist in the subducting Pacific slab beneath Japan (Tono *et al.* 2009), it is difficult to distinguish the anisotropy in the Pacific slab from the shear-wave splitting measurements. Dry olivine is dominant in the oceanic lithospheric mantle because the water prefers to dissolve in melting when it formed (e.g. Hirth & Kohlstedt 1996; Keppler & Bolfan-Casanova 2006; Grant *et al.* 2007).

The B-type olivine fabric could be produced by high pressure with low H_2O fugacity as well as by high H_2O fugacity at low pressure (e.g. Mainprice *et al.* 2005; Jung 2009; Ohuchi *et al.* 2011). Eberhart-Phillips & Reyners (2009) suggested that the B-type olivine fabric could be formed in an oceanic plate by great yielding before it bends down at the trench, but the B-type fabric cannot be developed in a young plate because of its easy yielding. This suggestion is consistent with the trench-parallel azimuthal anisotropy in the very old Pacific slab under Tohoku, the old PHS slab under South Kyushu, as well as the trench-normal azimuthal anisotropy in the young Pacific slab under Alaska.

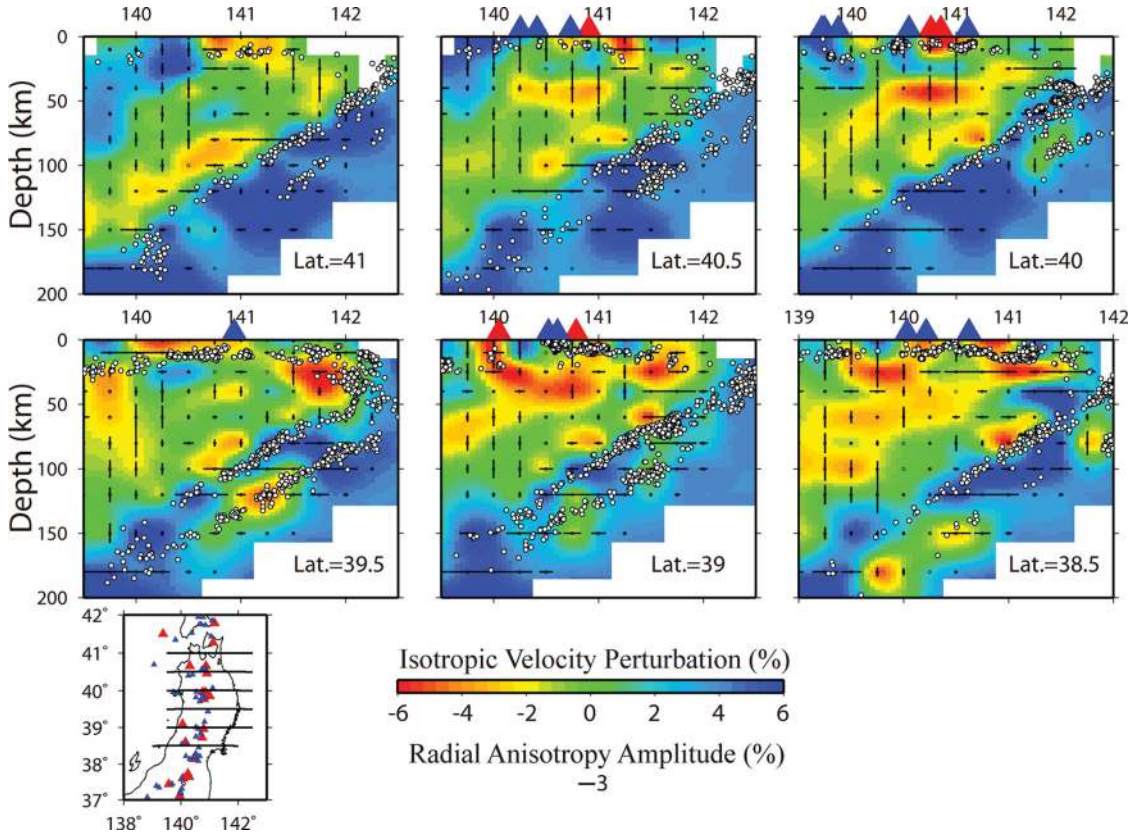

Figure 9. Vertical cross-sections of *P*-wave radial anisotropy tomography under Tohoku along the profiles as shown on the inset map. The red and blue colours denote low and high isotropic-velocity anomalies, respectively. The horizontal bars denote that the horizontal velocity is greater than the vertical velocity at each grid node, whereas the vertical bars denote that the vertical velocity is greater than the horizontal velocity at each grid node. The bar length denotes the radial anisotropy amplitude; its scale is shown at the bottom. The red and blue triangles denote the active and quaternary volcanoes, respectively. The white dots denote the seismicity that occurred within a 10 km width along each profile.

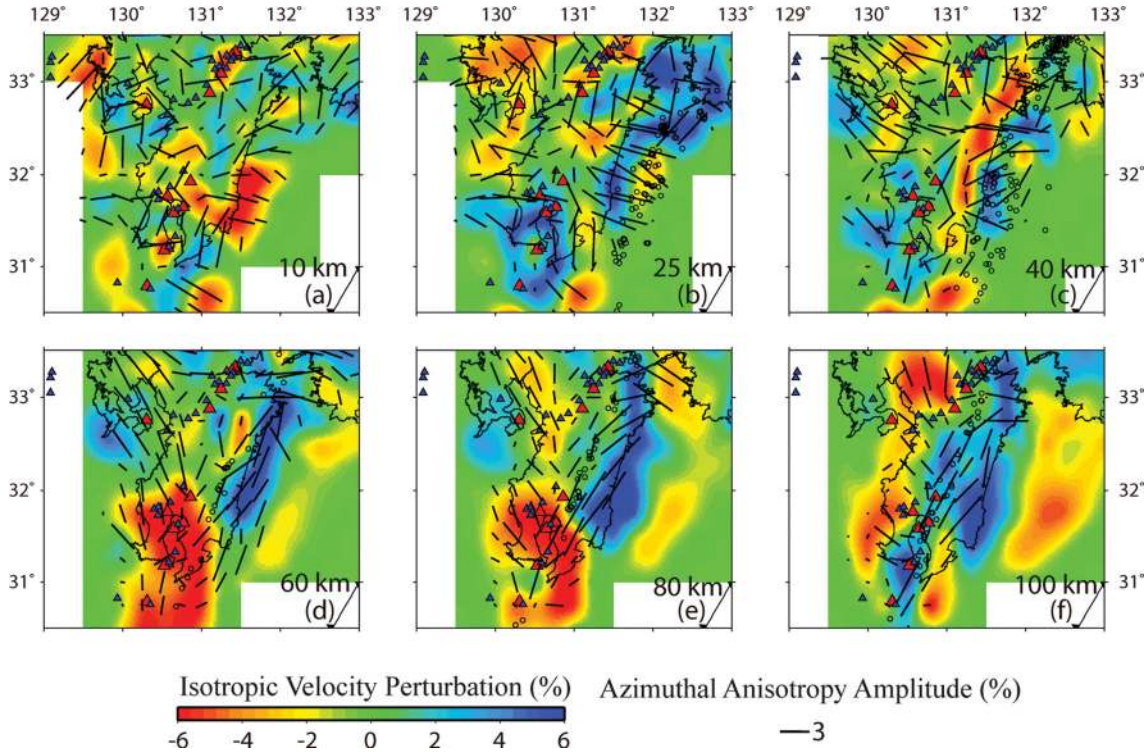

Figure 10. The same as Fig. 6 but for *P*-wave azimuthal anisotropy tomography in Kyushu. The open circles denote the seismicity that occurred within 10 km depth of each layer.

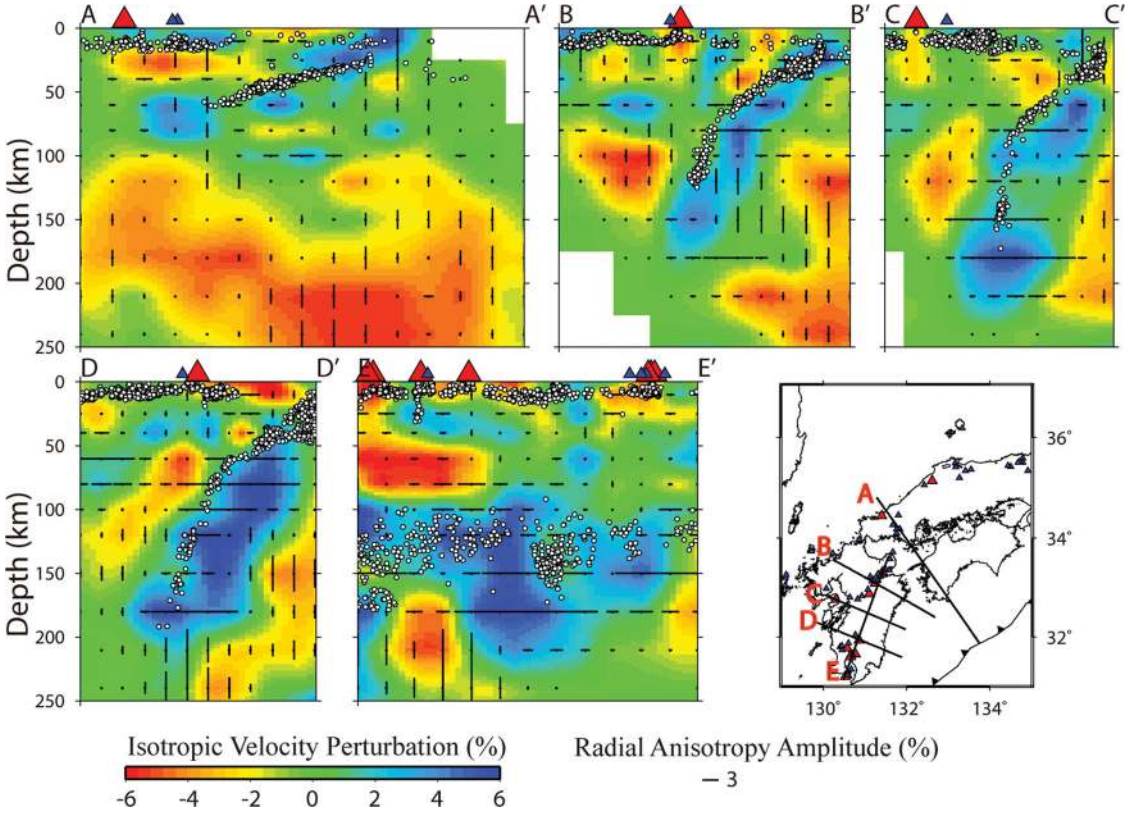

Figure 11. The same as Fig. 9 but for *P*-wave radial anisotropy tomography under Kyushu.

5.3 Radial anisotropy of the subduction zones

We assume that the properties of radial anisotropy for *P*-wave are similar to those for *S*-wave. Similar to the use of V_{sh}/V_{sv} ratio in surface-wave tomography studies (e.g. Nettles & Dziewonski 2008; Fichtner *et al.* 2010; Yuan *et al.* 2011), here we use V_{ph}/V_{pv} ratio to express the *P*-wave radial anisotropy obtained by this study. Our results (Figs 9 and 11) show similar *P*-wave radial anisotropy in Tohoku and Kyushu, that is, negative radial anisotropy ($V_{ph}/V_{pv} < 1$) is dominant in the mantle-wedge low-V zones, while positive radial anisotropy ($V_{ph}/V_{pv} > 1$) appears in the high-V subducting slabs. Our these results agree well with the traditional paradigm in the geodynamic interpretation of upper mantle anisotropy with $V_{sh}/V_{sv} > 1$ for horizontal flow and $V_{sh}/V_{sv} < 1$ for vertical flow, due to A-type olivine LPO after large-strain deformation (e.g. Nicolas & Christensen 1987; Savage 1999; Park & Levin 2002).

However, many studies have revealed transitions of olivine fabrics induced by temperature, pressure and water content (e.g. Durham & Goetze 1977; Nicolas & Christensen 1987; Mainprice *et al.* 2005; Karato *et al.* 2008; Jung *et al.* 2009). The low-V anomalies in the mantle wedge beneath the arc volcanoes are related to the arc magmatism induced by the slab dehydration and mantle-wedge corner flow (e.g. Stern 2002; Hasegawa *et al.* 2005; Zhao *et al.* 2011a,b). Thus, the olivine LPO may change from A-, to E- or C-type in the mantle wedge and to B-type in the forearc mantle wedge induced by the presence of water (Karato *et al.* 2008). The negative radial anisotropy in low-V zones beneath the arc volcanoes (perhaps upwelling flows) is consistent with the E-type olivine LPO ($V_{sh}/V_{sv} < 1$ in vertical flow), but inconsistent with the C-type olivine LPO ($V_{sh}/V_{sv} > 1$ and weak in vertical flow). Karato *et al.* (2008) showed details of the relation between the olivine fabrics and seismic anisotropy in different cases of mantle flow. Our results of *P*-wave radial anisotropy suggest that the E-type olivine may be dominant in the mantle upwelling beneath the arc volcanoes in Tohoku and Kyushu, being consistent with the observations that some samples in the island arc environments show E-type fabrics (Mehl *et al.* 2003; Sawaguchi 2004).

In the mantle upwelling related to arc magmatism, much of the water may be removed from olivine to melts (e.g. Karato 1986; Grant *et al.* 2007). As a result, E-type (rather than C-type) olivine may be dominant in the upwelling flow in the mantle wedge. The upwelling beneath the subducting PHS slab in Kyushu is induced by the corner flow in the big mantle wedge above the Pacific slab in the mantle transition zone as well as the deep dehydration of the Pacific slab (Ohtani *et al.* 2004; Ohtani & Zhao 2009; Wang & Zhao 2012; Zhao *et al.* 2012). Thus the E-type olivine LPO may be the main contributor to the negative radial anisotropy in the upwelling. However, because of the high water content and higher temperature in the upper mantle under Kyushu, partial melting would distribute widely in the deep part of upper mantle there (Hirschmann 2006). Thus A-type olivine may be dominant in the upwelling below the subducting PHS slab in Kyushu due to much water releasing from the olivine into melts. However, the situation is dependent on the contents of water and partial melts (Karato *et al.* 2008). The negative radial anisotropy in the mantle upwelling below the PHS slab is similar to the observed $V_{sv}/V_{sh} > 1$ anisotropy in the deep portion of mantle plume (>100 km depth) beneath Iceland (Gaherty 2001). In contrast, the positive radial anisotropy in the subducting Pacific slab under Tohoku and in the PHS slab under Kyushu is consistent with the anisotropy induced by A- or B-type olivine LPO.

6 CONCLUSIONS

Using a large number of high-quality arrival-time data from local shallow and intermediate-depth earthquakes, we determined

high-resolution *P*-wave tomography for 3-D azimuthal and radial anisotropy in the crust and upper mantle under Tohoku and Kyushu. Main results of this work are summarized as follows.

1. In the upper crust, *P*-wave azimuthal anisotropy is complex in the backarc area, whereas it is generally trench-parallel in the forearc area beneath Tohoku, which is consistent with shear-wave splitting measurements in the region. This result suggests that *P*-wave azimuthal anisotropy in the upper crust could be estimated reliably by high-resolution tomographic imaging.

2. Trench-parallel azimuthal anisotropy with amplitude of <4 per cent is visible in the forearc mantle wedge beneath Tohoku and Kyushu, suggesting that B-type olivine fabrics is dominant there.

3. Trench-parallel azimuthal anisotropy in the mantle wedge under the volcanic front area exists in Tohoku but not in Kyushu. The anisotropy may be induced by 3-D flow in the mantle wedge, and the 3-D flow can be developed if the subduction rate of the oceanic plate is large enough.

4. Trench-parallel azimuthal FVDs and positive radial anisotropy (i.e. horizontal velocity > vertical velocity) are revealed in both the Pacific slab beneath Tohoku and the PHS slab beneath Kyushu. There are two possibilities for the cause of the slab anisotropy. One is that the slabs contain mainly A-type olivine, and they keep the original fossil anisotropy formed at the mid-ocean ridge. The other possibility is that B-type olivine is dominant in the slabs.

5. Negative radial anisotropy (i.e. vertical velocity > horizontal velocity) appears in the low-V zones in the mantle wedge under the arc volcanoes and backarc areas in Tohoku and Kyushu, which may reflect the E-type olivine LPO in the upwelling flow. Negative radial anisotropy is also revealed in the low-V zones below the subducting PHS slab in Kyushu, which may reflect the E-type or A-type olivine LPO in the upwelling flow in the big mantle wedge above the Pacific slab under western Japan.

ACKNOWLEDGEMENTS

We thank the data center of the Kiban seismic network and the JMA unified catalogue for providing the high-quality data used in this study. Part of the data was collected carefully by the staffs of Research Center for Prediction of Earthquakes and Volcanic Eruptions, Tohoku University from all the available raw seismograms. Prof. Andrea Morelli (the Editor) and two anonymous reviewers provided thoughtful review comments and suggestions that have improved the manuscript. We thank Drs. Liang Zhao, Xiaoge Huang and M. Ishise for thoughtful discussions. This work was supported by grants from the National Science Foundation of China to J. Wang (Nos. 41274089, 41074060 and 40974026) and grants from Japan Society for the Promotion of Science to D. Zhao (Kiban-A 17204037 and Kiban-S 11050123), as well as by the Global-COE program of Earth and Planetary Sciences of Tohoku University. The figures were made using the GMT software (Wessel & Smith 1998).

REFERENCES

Anderson, D. & Dziewonski, A., 1982. Upper mantle anisotropy: evidence from free oscillation, *Geophys. J. R. astr. Soc.,* **69,** 383–404.

Backus, G.E., 1965. Possible forms of seismic anisotropy of uppermost mantle under oceans, *J. geophys. Res.,* **70,** 3429–3439.

Barclay, A.H., Toomey, D.R. & Solomon, S.C., 1998. Seismic structure and crustal magmatism at the Mid-Atlantic Ridge, 35 degrees N, *J. geophys. Res.,* **103,** 17 827–17 844.

Behn, M.D., Hirth, G. & Kelemen, P.B., 2007. Trench-parallel anisotropy produced by foundering of arc lower crust, *Science,* **317,** 108–111.

Bostock, M.G., Hyndman, R.D., Rondenay, S. & Peacock, S.M., 2002. An inverted continental Moho and serpentinization of the forearc mantle, *Nature,* **417,** 536–538.

Boudier, F., Baronnet, A. & Mainprice, D., 2010. Serpentine mineral replacements of natural olivine and their seismic implications: oceanic lizardite versus subduction-related antigorite, *J. Petrol.,* **51,** 495–512.

Capdeville, Y., Guillot, L. & Marigo, J.J., 2010. 2-D non-periodic homogenization to upscale elastic media for P-SV waves, *Geophys. J. Int.,* **182,** 903–922.

Carlson, R.L. & Miller, D.J., 2003. Mantle wedge water contents estimated from seismic velocities in partially serpentinized peridotites, *Geophys. Res. Lett.,* **30,** 1250, doi:10.1029/2002GL016600.

Cheng, B., Zhao, D. & Zhang, G., 2011. Seismic tomography and anisotropy in the source area of the 2008 Iwate-Miyagi earthquake (M 7.2), *Phys. Earth planet. Inter.,* **184,** 172–185.

Christensen, N.I., 1984. The magnitude, symmetry and origin of upper mantle anisotropy based on fabric analyses of ultramafic tectonites, *Geophys. J. R. astr. Soc.,* **76,** 89–111.

Christensen, N.I., 2004. Serpentinites, peridotites, and seismology, *Int. Geol. Rev.,* **46,** 795–816.

Crampin, S., 1984. Effective anisotropic constants for wave-propagation through cracked solids, *Geophys. J. R. astr. Soc.,* **76,** 135–145.

Couvy, H., Frost, D.J., Heidelbach, F., Nyilas, K., Ungar, T., Mackwell, S. & Cordier, P., 2004. Shear deformation experiments of forsterite at 11GPa-1400 degrees C in the multianvil apparatus, *Eur. J. Mineral.,* **16,** 877–889.

Durham, W.B. & Goetze, C., 1977. Plastic-flow of oriented single-crystals of olivine – 1. Mechanical data, *J. geophys. Res.,* **82,** 5737–5753.

Eberhart-Phillips, D. & Henderson, C.M., 2004. Including anisotropy in 3-D velocity inversion and application to Marlborough, New Zealand, *Geophys. J. Int.,* **156,** 237–254.

Eberhart-Phillips, D. & Reyners, M., 2009. Three-dimensional distribution of seismic anisotropy in the Hikurangi subduction zone beneath the central North Island, New Zealand, *J. geophys. Res.,* **114,** B06301, doi:10.1029/2208jb005947.

Engdahl, E.R. & Lee, W.H.K., 1976. Relocation of local earthquakes by seismic ray tracing, *J. geophys. Res.,* **81,** 4400–4406.

Faccenda, M., Burlini, L., Gerya, T.V. & Mainprice, D., 2008. Fault-induced seismic anisotropy by hydration in subducting oceanic plates, *Nature,* **455,** 1097–1098.

Fichtner, A., Kennett, B.L.N., Igel, H. & Bunge, H.P., 2010. Full waveform tomography for radially anisotropic structure: new insights into present and past states of the Australasian upper mantle, *Earth planet. Sci. Lett.,* **290,** 270–280.

Gaherty, J.B., 2001. Seismic evidence for hotspot-induced buoyant flow beneath the Reykjanes Ridge, *Science,* **293,** 1645–1647.

Grant, K.J., Brooker, R.A., Kohn, S.C. & Wood, B.J., 2007. The effect of oxygen fugacity on hydroxyl concentrations and speciation in olivine: implications for water solubility in the upper mantle, *Earth planet. Sci. Lett.,* **261,** 217–229.

Hall, C.E., Fischer, K.M., Parmentier, E.M. & Blackman, D.K., 2000. The influence of plate motions on three-dimensional back arc mantle flow and shear wave, *J. geophys. Res.,* **105,** 28 009–28 033.

Hasegawa, A., Nakajima, J., Umino, N. & Miura, S., 2005. Deep structure of the northeastern Japan arc and its implications for crustal deformation and shallow seismic activity, *Tectonophysics,* **403,** 59–75.

Hearn, T.M., 1996. Anisotropic Pn tomography in the western United States, *J. geophys. Res.,* **101,** 8403–8414.

Hess, H.H., 1964. Seismic anisotropy of uppermost mantle under oceans, *Nature,* **203,** 629–631.

Hirschmann, M.M., 2006. Water, melting, and the deep Earth H(2)O cycle, *Annu. Rev. Earth planet. Sci.,* **34,** 629–653.

Hirth, G. & Kohlstedt, D.L., 1996. Water in the oceanic upper mantle: implications for rheology, melt extraction and the evolution of the lithosphere, *Earth planet. Sci. Lett.,* **144,** 93–108.

Holtzman, B.K., Kohlstedt, D.L., Zimmerman, M.E., Heidelbach, F., Hiraga, T. & Hustoft, J., 2003. Melt segregation and strain partitioning: implications for seismic anisotropy and mantle flow, *Science,* **301,** 1227–1230.

Honda, S. & Yoshida, T., 2005. Application of the model of small-scale convection under the island arc to the NE Honshu subduction zone, *Geochem. Geophys. Geosyst.,* **6,** Q01002, doi:10.1029/2004gc000785.

Huang, Z.C., Zhao, D.P. & Wang, L.S., 2011a. Shear wave anisotropy in the crust, mantle wedge, and subducting Pacific slab under northeast Japan, *Geochem. Geophys. Geosyst.,* **12,** Q01002, doi:10.1029/2010gc003343.

Huang, Z.C., Zhao, D.P. & Wang, L.S., 2011b. Frequency-dependent shear-wave splitting and multilayer anisotropy in Northeast Japan, *Geophys. Res. Lett.,* **38,** L08302, doi:10.1029/2011gl046804.

Huang, Z.C., Zhao, D.P. & Wang, L.S., 2011c. Seismic heterogeneity and anisotropy of the Honshu arc from the Japan Trench to the Japan Sea, *Geophys. J. Int.,* **184,** 1428–1444.

Hyndman, R.D. & Peacock, S.M., 2003. Serpentinization of the forearc mantle, *Earth planet. Sci. Lett.,* **212,** 417–432.

Ishise, M., Kawakatsu, H. & Shiomi, K., 2012. Revision of the 3-D anisotropic velocity structure of the Japan islands using Hi-net data: Northeastern Japan, B12–2, in *Programme and Abstracts of the 2012 Fall Meeting of Seismological Society of Japan,* Hakodate, Japan.

Ishise, M. & Oda, H., 2005. Three-dimensional structure of P-wave anisotropy beneath the Tohoku district, northeast Japan, *J. geophys. Res.,* **110,** B07304, doi:10.1029/2004jb003599.

Jeffreys, H. & Bullen, K., 1940. *Seismological Tables,* British Association for the Advancement of Science, London, 50 pp.

Jull, M. & Kelemen, P.B., 2001. On the conditions for lower crustal convective instability, *J. geophys. Res.,* **106,** 6423–6446.

Jung, H., 2009. Deformation fabrics of olivine in Val Malenco peridotite found in Italy and implications for the seismic anisotropy in the upper mantle, *Lithos,* **109,** 341–349.

Jung, H. & Karato, S., 2001. Water-induced fabric transitions in olivine, *Science,* **293,** 1460–1463.

Jung, H., Katayama, I., Jiang, Z., Hiraga, I. & Karato, S., 2006. Effect of water and stress on the lattice-preferred orientation of olivine, *Tectonophysics,* **421,** 1–22.

Jung, H., Mo, W. & Green, H.W., 2009. Upper mantle seismic anisotropy resulting from pressure-induced slip transition in olivine, *Nat. Geosci.,* **2,** 73–77.

Karato, S., 1986. Does partial melting reduce the creep strength of the upper mantle? *Nature,* **319,** 309–310.

Karato, S., Jung, H., Katayama, I. & Skemer, P., 2008. Geodynamic significance of seismic anisotropy of the upper mantle: new insights from laboratory studies, *Annu. Rev. Earth planet. Sci.,* **36,** 59–95.

Katayama, I., Hirauchi, H., Michibayashi, K. & Ando, J., 2009. Trench-parallel anisotropy produced by serpentine deformation in the hydrated mantle wedge, *Nature,* **461,** 1114–1117.

Katayama, I., Jung, H. & Karato, S.I., 2004. New type of olivine fabric from deformation experiments at modest water content and low stress, *Geology,* **32,** 1045–1048.

Katayama, I. & Karato, S., 2006. Effect of temperature on the B- to C-type olivine fabric transition and implication for flow pattern in subduction zones, *Phys. Earth planet. Int.,* **157,** 33–45.

Kay, R.W. & Kay, S.M., 1991. Creation and destruction of lower continental-crust, *Geol. Rundsch*., **80,** 259–278.

Kelemen, P.B., Rilling, J.L., Parmentier, E.M., Mehl, L. & Hacker, B.R., 2003. Thermal structure due to solid-state flow in the mantle wedge beneath arcs, in *Inside the Subduction Factory,* pp. 293–311, ed. Eiler, E.J., AGU Monograph.

Keppler, H. & Bolfan-Casanova, N., 2006. Thermodynamics of water solubility and partitioning, *Rev. Mineral .Geochem.,* **62,** 193–230.

Kern, H., Liu, B. & Popp, T., 1997. Relationship between anisotropy of P and S wave velocities and anisotropy of attenuation in serpentinite and amphibolite, *J. geophys. Res.,* **102,** 3051–3065.

Kincaid, C. & Griffiths, R.W., 2003. Laboratory models of the thermal evolution of the mantle during rollback subduction, *Nature,* **425,** 58–62.

Kneller, E.A., van Keken, P.E., Karato, S. & Park, J., 2005. B-type olivine fabric in the mantle wedge: insights from high-resolution non-Newtonian subduction zone models, *Earth planet. Sci. Lett.,* **237,** 781–797.

Liu, X., Zhao, D. & Li, S., 2013. Seismic imaging of the Southwest Japan arc from the Nankai trough to the Japan Sea, *Phys. Earth planet. Inter.,* **216,** 59–73.

Long, M.D. & Silver, P.G., 2008. The subduction zone flow field from seismic anisotropy: a global view, *Science,* **319,** 315–318.

Long, M.D. & van der Hilst, R.D., 2005. Upper mantle anisotropy beneath Japan from shear wave splitting, *Phys. Earth planet. Int.,* **151,** 206–222.

Mainprice, D., 2007. 2.16 – seismic anisotropy of the deep Earth from a mineral and rock physics perspective, in *Treatise on Geophysics,* pp. 437–491, ed. Gerald, S., Elsevier, Amsterdam.

Mainprice, D., Tommasi, A., Couvy, H., Cordier, P. & Frost, D.J., 2005. Pressure sensitivity of olivine slip systems and seismic anisotropy of Earth's upper mantle, *Nature,* **433,** 731–733.

Maupin, V. & Park, J., 2007. 1.09-Theory and observations—wave propagation in anisotropic media, in *Treatise on Geophysics,* pp. 289–321, ed. Schubert, G., Elsevier, Amsterdam.

Mehl, L., Hacker, B.R., Hirth, G. & Kelemen, P.B., 2003. Arc-parallel flow within the mantle wedge: evidence from the accreted Talkeetna arc, south central Alaska, *J. geophys. Res.,* **108,** 2375, doi:10.1029/2002JB002233.

Mizukami, T., Wallis, S.R. & Yamamoto, J., 2004. Natural examples of olivine lattice preferred orientation patterns with a flow normal a-axis maximum, *Nature,* **427,** 432–436.

Morishige, M. & Honda, S., 2011. Three-dimensional structure of P-wave anisotropy in the presence of small-scale convection in the mantle wedge, *Geochem. Geophys. Geosyst.,* **12,** Q12010, doi:10.1029/2011gc003866.

Nakajima, J. & Hasegawa, A., 2004. Shear-wave polarization anisotropy and subduction-induced flow in the mantle wedge of northeastern Japan, *Earth planet. Sci. Lett.,* **225,** 365–377.

Nakajima, J., Shimizu, J., Hori, S. & Hasegawa, A., 2006. Shear-wave splitting beneath the southwestern Kurile arc and northeastern Japan arc: a new insight into mantle return flow, *Geophys. Res. Lett.,* **33,** L05305, doi:10.1029/2005gl025053.

Nettles, M. & Dziewonski, A.M., 2008. Radially anisotropic shear velocity structure of the upper mantle globally and beneath North America, *J. geophys. Res.,* **113,** B02303, doi:10.1029/2006jb004819.

Nicolas, A. & Christensen, N.I., 1987. Formation of anisotropy in upper mantle peridotites—a review, in *Composition, Structure and Dynamics of the Lithosphere-Asthenosphere System,* pp. 111–123, eds Fuchs, K. & Froidevaux, C., Am. Geophys. Un., Washington, DC.

Ohtani, E. & Zhao, D., 2009. The role of water in the deep upper mantle and transition zone: dehydration of stagnant slabs and its effects on the big mantle wedge, *Russ. Geol. Geophys.,* **50,** 1073–1078.

Ohtani, E., Litasov, K., Hosoya, T., Kubo, T. & Kondo, T., 2004. Water transport into the deep mantle and formation of a hydrous transition zone, *Phys. Earth planet. Int.,* **143,** 255–269.

Ohuchi, T., Kawazoe, T., Nishihara, Y., Nishiyama, N. & Irifune, T., 2011. High pressure and temperature fabric transitions in olivine and variations in upper mantle seismic anisotropy, *Earth planet. Sci. Lett.,* **304,** 55–63.

Paige, C.C. & Saunders, M.A., 1982. LSQR - an algorithm for sparse linear-equations and sparse least-squares, *Acm Trans. Math. Software,* **8,** 43–71.

Park, J. & Levin, V., 2002. Seismic anisotropy: tracing plate dynamics in the mantle, *Science,* **296,** 485–489.

Park, J. & Yu, Y., 1993. Seismic determination of elastic anisotropy and mantle flow, *Science,* **261,** 1159–1162.

Pozgay, S.H., Wiens, D.A., Conder, J.A., Shiobara, H. & Sugioka, H., 2007. Complex mantle flow in the Mariana subduction system: evidence from shear wave splitting, *Geophys. J. Int.,* **170,** 371–386.

Raitt, R.W., Shor, G.G., Francis, T.J.G. & Morris, G.B., 1969. Anisotropy of Pacific upper mantle, *J. geophys. Res.,* **74,** 3095–3109.

Raterron, P., Amiguet, E., Chen, J.H., Li, L. & Cordier, P., 2009. Experimental deformation of olivine single crystals at mantle pressures and temperatures, *Phys. Earth planet. Int.,* **172,** 74–83.

Raterron, P., Chen, J., Li', L., Weidner, D. & Cordier, P., 2007. Pressure-induced slip-system transition in forsterite: single-crystal rheological properties at mantle pressure and temperature, *Am. Mineral.,* **92,** 1436–1445.

Russo, R.M. & Silver, P.G., 1994. Trench-parallel flow beneath the Nazca plate from seismic anisotropy, *Science,* **263,** 1105–1111.
Salah, M.K., Seno, T. & Iidaka, T., 2009. Seismic anisotropy in the wedge above the Philippine Sea slab beneath Kanto and southwest Japan derived from shear wave splitting, *J. Asian Earth Sci.,* **34,** 61–75.
Savage, M.K., 1999. Seismic anisotropy and mantle deformation: what have we learned from shear wave splitting? *Rev. Geophys.,* **37,** 65–106.
Sawaguchi, T., 2004. Deformation history and exhumation process of the horoman Peridotite Complex, Hokkaido, Japan, *Tectonophysics,* **379,** 109–126.
Smith, G.P., Wiens, D.A., Fischer, K.M., Dorman, L.M., Webb, S.C. & Hildebrand, J.A., 2001. A complex pattern of mantle flow in the Lau backarc, *Science,* **292,** 713–716.
Stern, R.J., 2002. Subduction zones, *Rev. Geophys.,* **40,** 1012, doi:10.1029/2001RG000108.
Thomsen, L., 1986. Weak elastic anisotropy, *Geophysics,* **51,** 1954–1966.
Tian, Y. & Zhao, D.P., 2012. Seismic anisotropy and heterogeneity in the Alaska subduction zone, *Geophys. J. Int.,* **190,** 629–649.
Tong, P., Zhao, D. & Yang, D., 2011. Tomography of the 1995 Kobe earthquake area: comparison of finite-frequency and ray approaches, *Geophys. J. Int.,* **187,** 278–302.
Tong, P., Zhao, D. & Yang, D., 2012. Tomography of the 2011 Iwaki earthquake (M 7.0) and Fukushima nuclear power plant area, *Solid Earth,* **3,** 43–51.
Tono, Y., Fukao, Y., Kunugi, T. & Tsuboi, S., 2009. Seismic anisotropy of the Pacific slab and mantle wedge beneath the Japanese islands, *J. geophys. Res.,* **114,** B07307, doi:10.1029/2009jb006290.
Wang, J. & Zhao, D.P., 2008. P-wave anisotropic tomography beneath Northeast Japan, *Phys. Earth planet. Int.,* **170,** 115–133.
Wang, J. & Zhao, D.P., 2010. Mapping P-wave anisotropy of the Honshu arc from Japan Trench to the back-arc, *J. Asian Earth Sci.,* **39,** 396–407.
Wang, J. & Zhao, D.P., 2012. P-wave anisotropic tomography of the Nankai subduction zone in Southwest Japan, *Geochem. Geophys. Geosyst.,* **13,** Q05017, doi:10.1029/2012gc004081.
Wang, J. & Zhao, D.P., 2013. Crustal and uppermost mantle structure and seismotectonics of North China Craton, *Tectonophysics,* **582,** 177–187.
Watanabe, T., Kasami, H. & Ohshima, S., 2007. Compressional and shear wave velocities of serpentinized peridotites up to 200 MPa, *Earth Planets Space,* **59,** 233–244.
Weissel, J.K., Reading, H.G. & Stegena, L., 1981. Magnetic lineations in marginal basins of the Western Pacific, *Phil. Trans. R. Soc. Lond., A,* **300,** 223–247.
Wessel, P. & Smith, W., 1998. New, improved version of the Generic Mapping Tools released, *EOS, Trans. Am. geophys. Un.,* **79,** 579.
Xia, S.H., Zhao, D.P. & Qiu, X.L., 2008. Tomographic evidence for the subducting oceanic crust and forearc mantle serpentinization under Kyushu, Japan, *Tectonophysics,* **449,** 85–96.
Yuan, H., Romanowicz, B., Fischer, K.M. & Abt, D., 2011. 3-D shear wave radially and azimuthally anisotropic velocity model of the North American upper mantle, *Geophys. J. Int.,* **184,** 1237–1260.
Zhang, S.Q. & Karato, S., 1995. Lattice preferred orientation of olivine aggregates deformed in simple shear, *Nature,* **375,** 774–777.
Zhao, D.P., Hasegawa, A. & Horiuchi, S., 1992. Tomographic imaging of P and S wave velocity structure beneath Northeastern Japan, *J. geophys. Res.,* **97,** 19 909–19 928.
Zhao, D.P., Huang, Z., Umino, N., Hasegawa, A. & Yoshida, T., 2011a. Seismic imaging of the Amur-Okhotsk plate boundary zone in the Japan Sea, *Phys. Earth planet. Inter.,* **188,** 82–95.
Zhao, D.P., Wei, W., Nishizono, Y. & Inakura, H., 2011b. Low-frequency earthquakes and tomography in western Japan: insight into fluid and magmatic activity, *J. Asian Earth Sci.,* **42,** 1381–1393.
Zhao, D.P., Yanada, T., Hasegawa, A., Umino, N. & Wei, W., 2012. Imaging the subducting slabs and mantle upwelling under the Japan Islands, *Geophys. J. Int.,* **190,** 816–828.
Zhao, L. & Xue, M., 2010. Mantle flow pattern and geodynamic cause of the North China Craton reactivation: evidence from seismic anisotropy, *Geochem. Geophys. Geosyst.,* **11,** Q07010, doi:10.1029/2010GC003068.

SUPPORTING INFORMATION

Additional Supporting Information may be found in the online version of this article:

Figure S1. The coordinate system specifying a ray path (dashed line) and the symmetry axis (red line) for azimuthal anisotropy (a) and radial anisotropy (b). V is the propagation vector of a ray with incident angle i and azimuthal angle ϕ. θ is the angle between the propagation vector and the symmetry axis. The red line denotes the hexagonal symmetry axis for azimuthal anisotropy (a) and radial anisotropy (b). For the azimuthal anisotropy tomography, the azimuthal angle ψ' of the hexagonal symmetry axis is normal to the fast-velocity direction (FVD). For details, see Eberhart-Phillips & Henderson (2004), Wang & Zhao (2008) and Ishise *et al.* (2012).
Figure S2. Results of a checkerboard resolution test for *P*-wave azimuthal anisotropy in Kyushu. In the input model, isotropic velocity anomalies of ±4 per cent are assigned alternatively to the grid nodes, and the fast-velocity directions (FVDs) at two adjacent grid nodes are perpendicular to each other (22.5° and 112.5°) with anisotropic amplitude of 2.8 per cent. The damping parameters for anisotropic parameters are 2.0 in the four iterations during the tomographic inversion. The black and white circles denote low and high velocity perturbations, respectively. The azimuth and length of bars represent the FVD and azimuthal anisotropy amplitude, respectively. The scales are shown at the bottom.
Figure S3. Results of a synthetic test for *P*-wave azimuthal anisotropy in Tohoku. In the input model, isotropic velocity anomalies of ±4 per cent are assigned alternatively to the grid nodes but without azimuthal anisotropy. The black and white circles denote low and high velocity perturbations, respectively. The azimuth and length of bars represent the FVD and azimuthal anisotropy amplitude, respectively. The scales are shown at the bottom.
Figure S4. Results of a synthetic test for *P*-wave radial anisotropy in Tohoku. In the input model, isotropic velocity anomalies of ±4 per cent are assigned alternatively to the grid nodes but without radial anisotropy. Black and white circles denote low and high velocity perturbations, respectively. The horizontal bars denote that the horizontal velocity is greater than the vertical velocity at each grid node, whereas the vertical bars denote that the vertical velocity is greater than the horizontal velocity at each grid node. The length of bars denotes the radial anisotropy amplitude. The scales are shown at the bottom.
Figure S5. The same as Fig. S3 but for a synthetic test in Kyushu.
Figure S6. The same as Fig. S4 but for a synthetic test in Kyushu.
Figure S7. Results of a synthetic test for *P*-wave azimuthal anisotropy in Tohoku. In the input model, the FVDs at two adjacent grid nodes are perpendicular to each other (22.5° and 112.5°) with anisotropic amplitude of 2.8 per cent, but without isotropic velocity anomaly. The black and white circles denote low and high velocity perturbations, respectively. The azimuth and length of bars represent the FVD and azimuthal anisotropy amplitude, respectively. The scales are shown at the bottom.
Figure S8. Results of a synthetic test for *P*-wave radial anisotropy in Tohoku. In the input model, the radial anisotropy amplitude of ±3 per cent are assigned alternatively to the grid nodes but without isotropic velocity anomaly. Black and white circles denote low and high velocity perturbations, respectively. The horizontal bars denote that the horizontal velocity is greater than the vertical velocity at each grid node, whereas the vertical bars denote that the vertical velocity is greater than the horizontal velocity at each grid

node. The length of bars denotes the radial anisotropy amplitude. The scales are shown at the bottom.

Figure S9. The same as Fig. S7 but for a synthetic test in Kyushu.

Figure S10. The same as Fig. S8 but for a synthetic test in Kyushu.

Figure S11. Results of a synthetic test for *P*-wave azimuthal anisotropy in Tohoku. The input model is the obtained tomographic result as shown in Fig. 6. Red and blue colors denote low and high isotropic-velocity anomalies, respectively. The azimuth and length of each bar represent the *P*-wave fast-velocity direction (FVD) and the anisotropy amplitude, respectively. The red curved lines show the upper boundary of the subducting Pacific slab at each depth. Red and blue triangles denote the active and quaternary volcanoes, respectively. The scales are shown at the bottom.

Figure S12. Result of a synthetic test for radial anisotropy in Tohoku. The input model is the obtained tomographic result as shown in Fig. 9. The red and blue colors denote low and high isotropic-velocity anomalies, respectively. The horizontal bars denote that the horizontal velocity is greater than the vertical velocity at each grid node, whereas the vertical bars denote that the vertical velocity is greater than the horizontal velocity at each grid node. The bar length denotes the radial anisotropy amplitude; its scale is shown at the bottom. The red and blue triangles denote the active and quaternary volcanoes, respectively. The white dots denote the seismicity that occurred within a 10 km width along each profile.

Figure S13. The same as Fig. S11 but for a synthetic test in Kyushu. The input model is the obtained tomographic result as shown in Fig. 10.

Figure S14. The same as Fig. S12 but for a synthetic test in Kyushu. The input model is the obtained tomographic result as shown in Fig. 11.

Figure S15. The Input model of a synthetic test for *P*-wave radial anisotropy tomography in Tohoku. In the input model, the distribution of 3-D isotropic velocity is the same as that of the real inversion result (Fig. 9) but the pattern of radial anisotropy is opposite to that appearing in the real inversion result, that is, positive radial anisotropy is assigned to the grid nodes with low velocity, while negative radial anisotropy is assigned to the grid nodes with high velocity. The amplitude of radial anisotropy assigned to all the grid nodes is ± 3 per cent. The red and blue colors denote low and high isotropic-velocity anomalies, respectively. The horizontal bars denote that the horizontal velocity is greater than the vertical velocity at each grid node, whereas the vertical bars denote that the vertical velocity is greater than the horizontal velocity at each grid node. The bar length denotes the radial anisotropy amplitude. The scales are shown at the bottom. The red and blue triangles denote the active and quaternary volcanoes, respectively. The white dots denote the seismicity that occurred within a 10 km width along each profile.

Figure S16. The same as Fig. S15 but for the input model of a synthetic test in Kyushu.

Figure S17. The inversion result of a synthetic test for *P*-wave radial anisotropy tomography in Tohoku. The input model is shown in Fig. S15. The red and blue colours denote low and high isotropic-velocity anomalies, respectively. The horizontal bars denote that the horizontal velocity is greater than the vertical velocity at each grid node, whereas the vertical bars denote that the vertical velocity is greater than the horizontal velocity at each grid node. The bar length denotes the radial anisotropy amplitude. The scales are shown at the bottom. The red and blue triangles denote the active and quaternary volcanoes, respectively. The white dots denote the seismicity that occurred within a 10 km width along each profile.

Figure S18. The same as Fig. S17 but for a synthetic test in Kyushu. The input model is shown in Fig. S16.

AZIMUTH_TOHOKU_20121222.ZIP: The compressed file for AZIMUTH_ TOHOKU_20121222.OUT, which is the results of the inverted 3-D P-wave azimuthal anisotropy of the Tohoku subduction zone. The values denote latitude, longitude, depth, isotropic-velocity anomaly, fast-velocity direction (azimuth) and azimuthal anisotropy amplitude, respectively, at every grid nodes.

AZIMUTH_SWJP_20121222.ZIP: The compressed file for AZIMUTH_SWJP_ 20121222.OUT, which is the results of the inverted 3-D P-wave azimuthal anisotropy in Southwest Japan (including Kyushu). The values denote latitude, longitude, depth, isotropic-velocity anomaly, fast-velocity direction (azimuth) and azimuthal anisotropy amplitude, respectively, at every grid nodes.

RADIAL_TOHOKU_20121222.ZIP: The compressed file for RADIAL_ TOHOKU_20121222.OUT, which is the results of the inverted 3-D P-wave radial anisotropy of the Tohoku subduction zone. The values denote latitude, longitude, depth, isotropic-velocity anomaly, and radial anisotropy amplitude, respectively, at every grid nodes. Positive radial anisotropy denotes that the horizontal velocity is greater than the vertical velocity at each grid node, i.e. $V_{ph}/V_{pv} > 1$. Negative radial anisotropy denotes that the vertical velocity is greater than the horizontal velocity at each grid node, i.e. $V_{ph}/V_{pv} < 1$.

RADIAL_SWJP_20121222.ZIP: The compressed file for RADIAL_SWJP_ 20121222.OUT, which is the results of the inverted 3-D P-wave radial anisotropy in Southwest Japan (including Kyushu). The values denote latitude, longitude, depth, isotropic-velocity anomaly, and radial anisotropy amplitude, respectively, at every grid nodes. Positive radial anisotropy denotes that the horizontal velocity is greater than the vertical velocity at each grid node, i.e. $V_{ph}/V_{pv} > 1$. Negative radial anisotropy denotes that the vertical velocity is greater than the horizontal velocity at each grid node, i.e. $V_{ph}/V_{pv} < 1$ (http://gji.oxfordjournals.org//lookup/supp1/doi:10.1093/gji/ggt086/-/DC1).